

Appendix 1.

**Analysis of the Influence of O₂ “A” band absorption
on atmospheric correction of ocean color imagery**

by

Kuiyuan Ding and Howard R. Gordon

(In press in *Applied Optics*)

Acknowledgement

We are grateful to the National Aeronautics and Space Administration for support under Grant NAGW-273 and Contracts NAS5-31363 and NAS5-31743.

Abstract

Two satellite borne ocean color sensors scheduled for launch in the mid 1990's each have a spectral band (nominally 745–785 nm) that completely encompasses the O₂ A band at 762 nm. These spectral bands are to be used in atmospheric correction of the color imagery by assessing the aerosol contribution to the total radiance at the sensor. The effect of the O₂ band on the radiance measured at the satellite is studied using a line-by-line backward Monte Carlo radiative transfer code. As expected, if the O₂ absorption is ignored, unacceptably large errors in the atmospheric correction result. The effects of the absorption depend on the vertical profile of the aerosol. By assuming an aerosol profile — the base profile — we show that it is possible to remove most of the O₂ absorption effects from atmospheric correction in a simple manner. We also investigate the sensitivity of the results to the details of the assumed base profile and find that, with the exception of situations in which there are significant quantities of aerosol in the stratosphere, e.g., following volcanic eruptions or in the presence of thin cirrus clouds, the quality of the atmospheric correction depends only weakly on the base profile. Situations with high concentrations of stratospheric aerosol require additional information regarding vertical structure to utilize this spectral band in atmospheric correction; however, it should be possible to infer the presence of such aerosol by a failure of the atmospheric correction to produce acceptable water-leaving radiance in the red. An important feature of our method for removal of the O₂ absorption effects is that it allows the use of lookup tables that can be prepared in the absence of O₂ absorption using more efficient radiative transfer codes.

Introduction

The radiance L_w exiting the ocean in the visible carries information concerning the concentration of phytoplankton in near-surface waters. Phytoplankton are microscopic plants that through photosynthesis, i.e., they combine CO_2 (dissolved in the water) and water to produce carbohydrates, form the first link in the marine food chain. Their influence on the CO_2 makes knowledge of their spatial and temporal variability important in the global carbon cycle. The Coastal Zone Color Scanner¹ (CZCS) launched by NASA on Nimbus 7 in the fall of 1978 (and operational until mid 1986) acquired imagery over the oceans in four spectral bands centered at 443, 520, 550, and 670 nm, with spectral widths of approximately 20 nm. Gordon et al.² showed that the phytoplankton pigment concentration, C — the sum of the concentrations of chlorophyll a and its degradation product phaeophyton a — could be derived from this imagery after removing the effects of the atmosphere. The CZCS spectral bands were located in atmospheric “windows,” so the atmospheric effects were due almost entirely to scattering by molecules (Rayleigh scattering) and by aerosols. Except for a small variation due to changes in atmospheric surface pressure, the Rayleigh scattering contribution can be computed exactly.³ In contrast, the aerosol scattering is highly variable in space and time and must be determined from the imagery itself. This was effected by utilizing the band at 670 nm, where L_w is very small so the top of the atmosphere (TOA) radiance is due to the atmosphere, to assess the aerosol’s contribution there. The spectral variation was then estimated by either using regions in the imagery where $C \lesssim 0.25 \text{ mg/m}^3$ (clear water regions⁴ for which L_w is known in the green bands as well as the red band) or by assigning a nominal spectral variation^{5,6} based on experience and on the properties of maritime aerosols. However, each procedure required assumptions, preventing a totally deterministic correction.

With the success of the CZCS as a proof-of-concept mission several ocean color instruments are being prepared for launch: the sea-viewing wide-field-of-view sensor (SeaWiFS);⁷ the moderate resolution imaging spectroradiometer (MODIS);⁸ and the ocean color and temperature sensor (OCTS) on the advanced earth observation satellite (ADEOS) to be launched by Japan. To provide better atmospheric correction, these instruments have spectral bands in the near infrared NIR, where the ocean can be considered to be a Fresnel-reflecting medium that absorbs all photons penetrating

the surface. In the case of SeaWiFS and OCTS, the NIR bands are 40 nm wide and positioned at 765 and 865 nm in windows free of water vapor absorption. The rather large spectral widths were governed by the requirement for high signal-to-noise ratios. Thus, the 765 nm band on both sensors was forced to completely encompass the O₂ “A” absorption band at 762 nm. It was believed that correction for the $\sim 10\%$ absorption due to the O₂ “A” band would be possible. We have developed an approach to the correction of the 765 nm bands for both SeaWiFS and OCTS for O₂ absorption and report such in this paper.

We begin with a brief review of the proposed⁹ atmospheric correction algorithm for SeaWiFS which utilizes the 765 nm band, and which ignores the presence of the O₂ absorption, i.e., was developed assuming the O₂ absorption feature in the 765 nm band did not exist. Next, through a series of Monte Carlo simulations, we examine the influence of the O₂ absorption on radiative transfer in the atmosphere. Based on these simulations a method for assessing and removing the O₂ effect is developed. Finally, we present examples of the performance of the end-to-end SeaWiFS atmospheric correction algorithm in the presence of the O₂ absorption.

The proposed SeaWiFS correction algorithm

In a recent paper, Gordon and Wang⁹ proposed an algorithm for the atmospheric correction of SeaWiFS, and ultimately, MODIS. Briefly, the total radiance $L_t(\lambda)$ measured at the top of the atmosphere at a wavelength λ can be decomposed as follows:

$$L_t(\lambda) = L_r(\lambda) + L_a(\lambda) + L_{ra}(\lambda) + t(\theta_v, \lambda)L_w(\lambda), \quad (1)$$

where $L_r(\lambda)$ is the radiance resulting from multiple scattering by air molecules (Rayleigh scattering) in the absence of aerosols, $L_a(\lambda)$ is the radiance resulting from multiple scattering by aerosols in the absence of the air, and $L_{ra}(\lambda)$ is the interaction term between molecular and aerosol scattering.¹⁰ In this equation, t is the diffuse transmittance of the atmosphere along the viewing direction specified by θ_v , the angle between the normal to the sea surface and the sensor.¹¹ Radiance arising from specular reflection of direct sunlight from the sea surface and subsequent propagation to the top of the atmosphere without scattering (sun glitter) has been ignored because SeaWiFS can be tilted away from the glitter pattern. However, specular reflection of skylight, created by both molecular

and aerosol scattering, is included in L_r , L_a , and L_{ra} . The influence of whitecaps has been ignored under the assumption that their contribution can be estimated from an estimate of the surface wind speed.¹²

The goal of the atmospheric correction is the retrieval of L_w from L_t . It is convenient to convert radiance (L) to a reflectance (ρ) defined to be $\pi L / F_0 \cos \theta_0$, where F_0 is the extraterrestrial solar irradiance, and θ_0 is the solar zenith angle. With this definition, Eq. (1) becomes

$$\rho_t(\lambda) = \rho_r(\lambda) + \rho_a(\lambda) + \rho_{ra}(\lambda) + t(\theta_v, \lambda)\rho_w(\lambda). \quad (2)$$

The reason for the particular decomposition in Eqs. (1) and (2) is that ρ_r can be computed exactly given the surface atmospheric pressure and λ .³

After computation of ρ_r , the algorithm utilizes $\rho_t - \rho_r = \rho_a + \rho_{ra}$ in the near infrared (NIR) at 765 and 865 nm, where ρ_w can be taken to be zero except in turbid coastal waters or possibly intense open-ocean coccolithophore blooms,¹³ to choose two aerosol models from a set of candidate models. The candidate models were taken from those proposed by Shettle and Fenn.¹⁴ The chosen aerosol models are then used to predict $\rho_a + \rho_{ra}$ in the visible which, when combined with ρ_r there, yields the desired $t\rho_w$. To assess the efficacy of the algorithm, simulations of ρ_t using aerosol models which were similar, but not identical, to the candidate aerosols models, were carried out. The simulated ρ_t was then used as pseudo data for insertion into the correction algorithm. The error $\Delta\rho$ in the retrieval of $t\rho_w$ at 443 nm was nearly always found to be $\lesssim 0.002$ and often $\lesssim 0.001$. This error meets the SeaWiFS goal of retrieving L_w (or ρ_w) at 443 nm to within $\sim \pm 5\%$ in waters with low phytoplankton pigment concentrations, e.g., the Sargasso Sea in summer.

The algorithm as described ignores the presence of the O_2 , i.e., in the simulations of ρ_t and ρ_r the model atmospheres were free of the O_2 absorption in the 765 nm band. In the presence of O_2 absorption ρ_t will be smaller in the 765 nm band than in its absence, so the computed value of $\rho_a + \rho_{ra}$ at 765 nm will be smaller. Operation of the present correction algorithm in the presence of the O_2 absorption with the smaller value of $\rho_a + \rho_{ra}$ will lead to the choice of an inappropriate model with which to determine $\rho_a + \rho_{ra}$ in the visible.

Our approach to dealing with the effects of the O_2 absorption in the 765 nm band is to use the value of $\rho_a + \rho_{ra}$ derived in the presence of the O_2 absorption to determine the value it would have were the O_2 absorption absent. The simulations presented below suggest that such an approach is viable.

Radiative transfer in the O_2 A band

In this section we describe the technique used to study the radiative transfer in the O_2 A band. What we wish to learn is the influence of the O_2 absorption on the reflectance ρ_t leaving the TOA in a band extending from 745 to 785 nm. Specifically, since the proposed SeaWiFS algorithm ignores the O_2 absorption, our goal is to be able to estimate what $\rho_a + \rho_{ra}$ would be in the absence of the absorption band.

A. The O_2 A band.

The O_2 A band extends from about 759 to 770 nm. There are 286 individual absorption lines having appreciable line strengths. Figure 1 shows a sample of the sea-level absorption coefficient as a function of wave number, $\nu = 1/\lambda$, computed from the positions, line strengths, and line widths of the individual absorption lines (assuming a Lorentz shape) taken from the AFGL compilation.¹⁵ Note that this figure covers only about 1.165 nm but contains 12 spectral lines, and the absorption coefficient varies from approximately 30 km^{-1} to about 0.2 km^{-1} over a small fraction of a nm. Because of the strong variation of the absorption coefficient with wavelength, the absorption over a band containing several lines will not be an exponential function of the path length. Thus, it is not possible to assign a single mean absorption coefficient to the entire O_2 A band. Furthermore, since the individual spectral lines are pressure and temperature broadened, even at discrete wavelengths, i.e., bands with width \ll the width of the individual spectral lines, the absorption coefficient will be dependent on altitude in the atmosphere. Thus, a complete treatment of the radiative transfer in this absorption band requires an atmosphere consisting of several layers in which the absorption coefficient is a very strong function of frequency.

B. Preliminary discussion of the O₂ effect.

It is possible to understand qualitatively the effect of the O₂ A band on the radiance exiting the top of the atmosphere by examining single scattering. First, we assume that the atmosphere is free of aerosols, i.e., we only have Rayleigh scattering and the scattering coefficient will vary with altitude in proportion to the density in the same manner as the O₂ abundance. For a given viewing geometry we define the air mass M as

$$M = \frac{1}{\cos \theta_v} + \frac{1}{\cos \theta_0},$$

where θ_0 is the solar zenith angle and θ_v is the viewing angle, i.e., the angle between the surface normal and the direction of propagation of the radiance exiting the TOA. Photons scattering from molecules at any altitude will have traversed a path of length proportional to M upon exiting the atmosphere. Thus, we expect the *decrease* in radiance exiting the atmosphere to be a function of M ; albeit *not* an exponential function. In the case of multiple scattering the path of the photon is no longer proportional to M so a similar argument does not apply; however, since the Rayleigh scattering optical thickness is small (~ 0.025) at 765 nm, multiple Rayleigh scattering will be small and the radiance decrease will still depend on M in much the same manner as for single scattering.

The addition of aerosols causes two complications: the aerosol concentration is a strong and variable function of altitude; and the aerosol concentration is usually sufficiently high that multiple scattering is significant. The influence of the vertical profile of the aerosol concentration is easy to understand in the single scattering approximation. Typically, over the oceans most of the aerosol is in the marine boundary layer which is 1-2 km thick. The aerosol component of the TOA radiance at 765 nm with a high concentration of aerosol in the boundary layer will be significantly larger than the molecular-scattering component. This radiance will have had to travel through most of the atmosphere (twice) before reaching the TOA. The total path is proportional to M , so we expect that the radiance decrease will be larger than that for an aerosol-free atmosphere (because more photons backscattered to the TOA will have had to travel farther in the atmosphere), and that it will be a function of the airmass. In contrast, if there is a high concentration of aerosol in the stratosphere, e.g., following a major volcanic eruption, a fraction of the TOA radiance will

have scattered from the stratosphere and not have traveled through a significant portion of the atmosphere. Then, for the same aerosol concentration as in the marine boundary layer example, the fractional decrease in the radiance due to the O_2 absorption will be less.

In general the aerosol will be distributed continuously throughout the atmosphere. A typical profile will display a high concentration in the boundary layer, a rapid decrease in the free troposphere and slower decrease in the background stratosphere, and occasionally an increase (sometimes large) due to recent (e.g., the past 1–3 years) volcanic activity.¹⁶ Thus, to simulate the fractional decrease in the TOA radiance near 765 nm due to the O_2 A band absorption requires an atmosphere composed of enough layers to adequately represent the vertical distribution of the aerosol.

C. The radiative transfer code and model.

The radiative transfer code we developed for this study is a backward Monte Carlo for a plane parallel atmosphere. Polarization of the light field is ignored. The backward procedure is used because it provides a significant increase in accuracy (over the forward Monte Carlo), for a given expense in computational time, when the radiance is desired in only a single viewing direction. In this kind of simulation, photons are ejected from the detector and followed to the sun. Actually, at each interaction in the atmosphere the probability that the photon will be scattered to the TOA in the direction of the sun is computed and used as the estimator. The atmosphere is bounded by the sea, which we model as a Fresnel reflecting surface that absorbs all photons that are transmitted through it. This is realistic because of the large absorption coefficient of liquid water in the NIR. The possibility that at any interaction a photon could be scattered toward the sea surface and be Fresnel-reflected back to the TOA is included in the Monte Carlo estimator. The code includes provision for the sea surface to be roughened by the wind with surface slopes obeying the Cox and Munk¹⁷ distribution; however, in all of the simulations presented here the surface was smooth.

For our model atmosphere we assumed that the density and temperature follow the U.S. 1976 Standard Atmosphere.¹⁸ O_2 is distributed in proportion to the atmospheric density. The individual O_2 spectral lines are assumed to have a Lorentz line shape. The line strengths and line widths

(at NTP) were taken from the AFGL¹⁵ compilation, and the line width varies with altitude in proportion to P/\sqrt{T} , where P is the pressure and T is the absolute temperature. The full width at half maximum (FWHM) at the sea surface of a typical absorption line in the A band is of the order of 0.1 cm^{-1} or $\sim 0.006 \text{ nm}$ (Figure 1). The atmosphere is composed of thirty-seven homogeneous layers. For each layer the O_2 absorption coefficient as a function of wave number ν was computed and tabulated at 10^5 values of ν between $\nu = 13,422.82 \text{ cm}^{-1}$ ($\lambda = 745 \text{ nm}$) and $12,738.85 \text{ cm}^{-1}$ ($\lambda = 785 \text{ nm}$). With this resolution, there are approximately 15 tabulated values within the FWHM of each absorption line at the surface. Linear interpolation is used for values of ν between tabulated values.

For a realistic treatment of the aerosol in the code, we further divide the atmosphere into four broad regions (Figure 2): (1) the marine boundary layer from the surface to 2 km, where the aerosol concentration is independent of altitude; (2) the free troposphere, where the aerosol concentrations varies in proportion to $\exp[-z/h]$, where z is the altitude (2-12 km) and h (called the scale height) is 2 km; (3) the background stratosphere (12-30 km), where the aerosol concentration is also exponential with a scale height of 5 km; and (4) a volcanic region (18-20 km) within the stratosphere that can contain a uniformly mixed volcanic aerosol. The optical properties of each of the four regions can be characterized by individual aerosol models, and any of the regions can be free of aerosols if desired. There is no aerosol above 30 km.

As in Ref. 9, the aerosol models used for the two lower regions were taken from Shettle and Fenn.¹⁴ Based on size distribution and composition measurements, they developed two models called the Tropospheric (to model the aerosol in the free troposphere — few large particles) and Oceanic (to model the aerosol produced by sea spray — few small particles). They combined these to form the Maritime model to represent the aerosol in the marine boundary layer. In terms of total aerosol number per unit volume, the Maritime model consists of 99% Tropospheric and 1% Oceanic. Gordon and Wang⁹ added a Coastal model (99.5% Tropospheric and 0.5% Oceanic) to provide a description of the aerosol that might be more representative of the boundary layer near the coast.

For the upper two regions we use a model for the background stratosphere from the WMO¹⁹ and a model for the volcanic aerosol from King et al.²⁰ Both models assume a 75% solution of H_2SO_4 . We have also included a volcanic ash model¹⁹ to represent fresh volcanic aerosol. The size distributions in these regions are modified gamma distributions.

With all of the optical properties of the atmosphere prescribed, the Monte Carlo code operates as follows. A photon is ejected from the receiver in a direction opposite to the observation direction with a wave number ν chosen from a uniform probability density over $12,738.82 \leq \nu \leq 13,422.82$ cm^{-1} . This choice of ν corresponds to assuming the extraterrestrial solar irradiance is constant over the this spectral interval, i.e., F_0 is replaced by its spectral band-averaged value. This is a convenience rather than a necessity. The Rayleigh optical extinction coefficient is then computed for ν based on Fenn et al.¹⁶ The aerosol extinction coefficient for each layer is provided by the aerosol model and concentration. It is assumed to be independent of λ over the 745–785 nm band. The optical distance (defined as $\int c(l) dl$, where $c(l)$ is the extinction coefficient along the path l) the photon travels is then determined from an exponential probability density function. From the tabulated values of the absorption and scattering coefficients, the physical distance that this corresponds to is determined, yielding the position of the first interaction point. The various estimators are computed, the photon allowed to scatter, and the process is repeated. In a typical computer run we trace the histories of 10^7 photons. This implies that there are approximately 1,300 photons sampling the FWHM of each individual O_2 absorption line at the sea surface.

D. Tests of the radiative transfer code.

Validation of the radiative transfer code was effected in two ways. In the absence of the O_2 absorption, the code was compared to the output of a successive order of scattering code similar to that used by Gordon and Wang.⁹ In this case, ν was not sampled, the molecular scattering was distributed uniformly from the surface to 100 km ($\tau_r = 0.0255$), and the aerosol scattering was uniformly distributed from the surface to 30 km ($\tau_a = 0.2$). The difference in the radiances computed by the two codes was usually $\lesssim 0.1\%$. This suggests that when the O_2 absorption features of the code are not employed, it is capable of returning radiances accurate to within 0.1%.

It is difficult to test completely the code’s handling of the O_2 absorption band, because, in contrast to the situation in the previous paragraph, we do not have a second, highly accurate code for comparison. However, the LOWTRAN²¹ atmospheric propagation code, which treats band absorption well, does have an approximate multiple scattering capability for calculating radiance reflected from the earth-atmosphere system.²² If aerosol scattering is omitted, at 765 nm multiple scattering effects should be small enough so that LOWTRAN can compute the radiance. Since LOWTRAN does not have the provision for a Fresnel-reflecting sea surface, we ran both codes with a totally absorbing lower boundary. The differences in the radiances (L_r) over the spectral band $12,735 \leq \nu \leq 13,425 \text{ cm}^{-1}$ between LOWTRAN and our code were $\sim 1\%$. Since our code treats both multiple scattering and gas absorption in a more precise manner than LOWTRAN, we believe this demonstrates that our code is satisfactory.

Finally, since the Lorentz line shape underestimates the absorption in the core of the lines and overestimates the absorption in the wings in the upper atmosphere ($z \gtrsim 10 \text{ km}$), we carried out a series of simulations using the Voigt²³ line shape to describe the O_2 absorption. For an aerosol-free atmosphere, the two line shapes yielded reflectances within the inherent error of the Monte Carlo procedure ($\sim 0.1\%$). The Lorentz line shape was used in the computations reported here.

Removal of O_2 A band absorption

In this section we develop the necessary relationships for removing the effects of the O_2 A band absorption from the 765 nm band. We shall use the notation that primes represent quantities computed or measured when the O_2 absorption band is *present* (*prime and present* both begin with “p”), and unprimed quantities represent those in the *absence* of the O_2 absorption. Thus Eq. (2) becomes

$$\begin{aligned}\rho_t - \rho_r &= \rho_a + \rho_{ra} \equiv \rho_A, \\ \rho'_t - \rho'_r &= \rho'_a + \rho'_{ra} \equiv \rho'_A,\end{aligned}\tag{3}$$

where we have explicitly used the fact that ρ_w is taken to be zero. The known quantities in these equations are ρ'_t (measured) and ρ_r . The SeaWiFS correction algorithm⁹ will employ precomputed lookup tables of ρ_r at standard atmospheric pressure, and ρ_A for a variety of aerosol models and optical thicknesses. As the notation suggests, these tables for the 765 nm SeaWiFS band have been

computed assuming that the O_2 absorption band does not exist. Thus, we need to find ρ_A from ρ'_t and ρ_r .

Our technique involves three steps: (1) finding ρ'_r from an empirical relationship between ρ'_r and ρ_r developed from simulations; (2) using the second equation in Eq. (3) to deduce ρ'_A ; and (3) finding ρ_A from an empirical relationship between ρ'_A and ρ_A developed from simulations. The desired ρ_A is then used in the atmospheric correction algorithm. A desirable feature of this O_2 correction is that both sets of O_2 -free lookup tables can still be employed. This is important because of the intense computational burden required for computing accurate reflectances in the presence of the O_2 absorption. In this section the empirical relationships we have mentioned above are developed.

A. Relationship between ρ_r and ρ'_r .

As described in an earlier section, we expect that the fractional decrease in the reflectance of the atmosphere-ocean system in the 745–785 nm spectral band due to the O_2 absorption will be a function of the two-way air mass M . Thus, we carried out a series of Monte Carlo simulations for an aerosol-free atmosphere using a variety of solar zenith and viewing angles. Both ρ_r and ρ'_r are computed, from which we found the fractional change in reflectance, $(\rho_r - \rho'_r)/\rho'_r$, as a function of M . The results are provided in Figure 3. Note that the minimum air mass is 2, and for this the O_2 absorption results in a decrease in the reflected radiance by approximately 7%. Typical viewing geometries have $2 \leq M \lesssim 5$, so the decrease in reflectance will vary between ~ 7 and $\sim 11\%$. The dotted line in Figure 3 is a least-squares fit of the computations to the air mass, i.e.,

$$\log_{10} \left(\frac{\rho_r - \rho'_r}{\rho'_r} \right) = a_{r0} + a_{r1}M + a_{r2}M^2 \equiv P_r(M),$$

where the a_{r0} , a_{r1} , and a_{r2} are -1.3491 , $+0.1155$, and -7.0218×10^{-3} , respectively. Using this fit, the desired ρ'_r for any M can be estimated from

$$\rho'_r = \left(1 + 10^{P_r(M)} \right)^{-1} \rho_r. \quad (4)$$

Figure 4 provides the error (%) in the estimated value of ρ'_r , using Eq. (4), for the simulations in Figure 3. It suggests that ρ'_r , the reflectance when the O_2 absorption is present, can be estimated from ρ_r , the reflectance in the absence of the O_2 absorption, to within $\sim \pm 0.2\%$ solely from the sun-viewing geometry.

B. Relationship between ρ_A and ρ'_A .

Now we develop a relationship between ρ_A and ρ'_A . We proceed in the same manner as with the Rayleigh component, i.e., we carry out a series of Monte Carlo simulations for an atmosphere including *both* aerosol and molecular scattering; however, there is an inherent difficulty in that the relationship cannot be independent of the vertical structure of the aerosol. Therefore, the estimate of ρ_A from ρ'_A will be less accurate than the estimation of ρ'_r from ρ_r . Clearly, we must choose an aerosol profile, on which to base the relationship, that is as representative as possible. We call this the “base” profile.

To assess the magnitude of the error in the relationship when an unrepresentative base profile is chosen, we begin with a very simple base profile and find the error in the prediction of ρ_A from ρ'_A . For this purpose, the base profile will consist of a uniformly mixed aerosol in the boundary layer (thickness of 2 km), with the free troposphere and stratosphere being free of aerosols. Thus all of the aerosol is in the marine boundary layer. The base aerosol optical thickness τ_a is taken to be 0.2693 and the aerosol model is the Shettle and Fenn¹⁴ Maritime model at 50% relative humidity (M50). Figure 5 provides $(\rho_A - \rho'_A)/\rho'_A$ as a function of M for a series of simulations using this base aerosol. As in the case of a pure Rayleigh scattering atmosphere, the line in Figure 5 is a least-squares fit of the computations to the air mass, i.e.,

$$\log_{10} \left(\frac{\rho_A - \rho'_A}{\rho'_A} \right) = a_{A0} + a_{A1} M + a_{A2} M^2 \equiv P_A(M), \quad (5)$$

where the a ’s are constants. Using this fit, the desired ρ_A for any M can be estimated from

$$\rho_A = \left(1 + 10^{P_A(M)} \right) \rho'_A. \quad (6)$$

We carried out simulations of ρ'_t for a set of aerosol profiles, concentrations, and type to test the accuracy with which ρ_A could be estimated given ρ'_t , if the three steps described at the beginning of this section were used. First we estimated ρ'_r from ρ_r using Eq. (4). This provided $\rho'_A = \rho'_t - \rho'_r$. Then we estimated ρ_A from ρ'_A using Eq. (6), based on their relationship in Figure 5, for the simple base profile. Figures 6 and 7 report the error, $\Delta\rho_A$, in this prediction of ρ_A from ρ'_t . In Figure 7 the Shettle and Fenn¹⁴ Tropospheric aerosol at 50% relative humidity (T50) has been used as the aerosol type in all layers, although the base aerosol was still M50. Two important conclusions can be drawn from the computations presented in these figures: (1) when the base profile is correct, the error in ρ_A is $\lesssim 0.5\%$ for $M \lesssim 5$, and nearly independent of the aerosol concentration and the aerosol type; and (2) even with the incorrect base profile, the error is usually $\lesssim 1\%$ as long as the test profile is not “too different” from the base profile (the case with a 5 km scale height in the free troposphere would be an example of a “too different” profile). This suggests that using the methodology described here, ρ_A can be derived from ρ'_t with an error $\lesssim 1\%$ as long as a realistic base aerosol profile is employed.

C. Choice of the base aerosol profile and type.

From the results presented above it is clear that it is important to use as realistic a base aerosol profile as possible. In fact, the computations suggest that the base profile should have some aerosol in the free troposphere and the stratosphere (unless these happen to be aerosol free) in order to be assured that the error in $\rho_A \lesssim 1\%$. With this in mind, we choose the base aerosol in the following manner. Referring to Figure 2, we use the Shettle and Fenn¹⁴ Maritime model with 80% relative humidity (M80) in the marine boundary layer, and their Tropospheric model with relative humidity of 50% (T50) for the free troposphere. The background stratospheric model¹⁹ (B) is proposed for the stratosphere. The volcanic component is taken to be absent in the base profile. The aerosol concentrations are adjusted so that when the visible range (defined¹⁴ to be 3.96 divided by the total extinction coefficient at 550 nm) is 25 km, the aerosol extinction coefficient is a continuous function of altitude, i.e., there is no discontinuous jump in the aerosol extinction from the top of the boundary layer to the bottom of the free troposphere of the type shown on the figure. Note, for any wavelength other than 550 nm, discontinuities in aerosol extinction will occur at the boundaries of

each region because the extinction coefficient for each region will have a different spectral variation. The base aerosol is denoted by M80-T50-B, which stands for M80 in the boundary layer, T50 in the free troposphere, and B in the stratosphere. Similar notation will be used for aerosol profiles through out the remainder of this paper. The $(\rho_A - \rho'_A)/\rho'_A - M$ relationship for this base aerosol profile is provided in Figure 8. Comparison with Figure 5 shows that for a given M , $(\rho_A - \rho'_A)/\rho'_A$ is slightly smaller (less O_2 absorption) than it is for the base profile with all of the aerosol in the marine boundary layer. For the M-80-T50-B base profile, the values of a_{A0} , a_{A1} , and a_{A2} in Eq. (5) are -1.0796 , $+9.0481 \times 10^{-2}$, and -6.8452×10^{-3} , respectively.

Application to atmospheric correction

In this section we apply the O_2 absorption correction scheme developed above to simulated ocean color data, e.g., SeaWiFS or OCTS. We will examine the optimum case, i.e., assume that the aerosol profile in the free troposphere and stratosphere is identical to the base profile. Only the aerosol in the boundary layer is allowed to be different from the base profile in concentration and/or in type. This of course would require knowing the free troposphere and stratospheric aerosol profile in advance.

We examined the following cases: (1) a visible range (VR) of 40 km, with the Maritime (M80) or Tropospheric (T80) aerosol at 80% relative humidity in the marine boundary layer; and (2) the same aerosol models with $VR = 15$ km. These correspond to either $\sim 40\%$ less (case 1) or $\sim 72\%$ more (case 2) aerosol in the boundary layer than in the base profile. The total and boundary-layer aerosol optical thicknesses for these models are provided in Tables 1–4.

Simulations were carried out for both ρ'_t and ρ_t so we could compare the performance of the algorithm in the presence and absence of the O_2 absorption to test the efficacy of the O_2 correction. The geometry of the simulations consisted of solar zenith angles $\theta_0 = 0(20^\circ)60^\circ$, with $\theta_v = 0^\circ$ and $\sim 45^\circ$ corresponding, respectively, to viewing at the scan center and the scan edge. All the simulations were carried out using the Monte Carlo code described above. The simulated value ρ'_t (in the presence of the O_2 absorption) at 765 nm was then combined with ρ_r through Eqs. (4) and (6) to estimate ρ_A , which was then used in the SeaWiFS correction algorithm. For comparison,

in the absence of the O_2 absorption, the simulated ρ_t was used in the normal way in the correction algorithm.⁹ The measure of effectiveness of the combined algorithm (O_2 removal and atmospheric correction) is the ability to recover $|t\rho_w|$ at 443 nm with an error of $\lesssim 0.002$. In this paper, the particular implementation of the algorithm provided in Ref. 9 utilizes the Maritime, Coastal, and Tropospheric models at relative humidities of 50%, 70%, 90%, and 99% as twelve candidate aerosol models. As in Ref. 9, it is assumed in this implementation that the aerosol is confined to the marine boundary layer.

Figures 9a-9d and 10a-10d show the error in the retrieved value of $t\rho_w$ (called $\Delta\rho$ on the figures) as a function of θ_0 and θ_v , for the four test cases: M80-T50-B and T80-T50-B with $VR = 15$ and 40 km. The open circles represent the error in the retrieval if the spectral band from 745 to 785 nm were free of O_2 absorption. Note that even if the O_2 absorption were absent, $\Delta\rho$ can at times be quite large. This owes to the fact that in the preparation of the lookup tables for implementation the SeaWiFS algorithm it was assumed that the aerosol was all in the marine boundary layer, i.e., a two-layer radiative transfer code (aerosols on the bottom) was employed. This assumption leads to errors when the aerosol is not confined near the surface. Even so, Figure 9 shows that when the aerosol optical depth at 443 is $\lesssim 0.4$ the correction error is within the desired range, i.e., ± 0.002 . In contrast, when the optical thickness at 443 reaches 0.7–0.8 (Figure 10), the error can become excessive. Measurements suggest that optical thicknesses in the latter range are not common when the aerosol is locally generated over the oceans.^{24,25} These simulations suggest that, even in the absence of the O_2 absorption, e.g., the atmospheric correction of MODIS, the assumptions made by Gordon and Wang⁹ may need to be modified by the addition of a third intermediate layer containing a mixture of aerosol and Rayleigh scatterers.

However, our main concern here is the efficacy of the removal of the effects of the O_2 absorption from the atmospheric correction. For this purpose we need only compare the differences between the open circles and the filled circles in Figures 9 and 10. We note that the difference is usually $\lesssim 0.001$ and often considerably less, indicating that the O_2 correction works reasonably well. Recall that if ρ_A is too small, an undercorrection will occur, i.e., the water-leaving reflectance at 443 will be too large ($\Delta\rho > 0$). Thus, in Figure 9, ρ_A is a little too large, while in Figure 10 it is

too small. This is consistent with the fact that the $(\rho_A - \rho'_A)/\rho'_A - M$ relationships in Figure 8 will move upward (more absorption) if the aerosol concentration in the boundary layer is increased and downward if the concentration is decreased with respect to the base profile. This implies that for the cases in Figure 10, $P_A(M)$ in Eq. (6) will lead to a value of ρ_A that is too small, while for the cases in Figure 9, the reverse is true.

To provide an appreciation of the magnitude of the O_2 effect that has been removed, in Table 5 we present the average $\Delta\rho$ over θ_0 for each model when the existence of the O_2 absorption is simply ignored and the proposed SeaWiFS algorithm operated using ρ'_t . Comparison with the results in Figures 9 and 10 suggest that we have removed about 97% of the error in the worst case (T80-T50-B at the scan edge).

In the simulated test of the O_2 absorption correction above, we used a base profile that was correct for the free troposphere and the stratosphere. This should be the optimum situation. To try to understand the effect of choosing an incorrect base profile on the end-to-end atmospheric correction algorithm, we computed $\Delta\rho$ using the base profile that was used in the preparation of Figure 5, i.e., a base profile assuming that all of the aerosol is in the boundary layer and modeled as M50. This is in contrast to the base profile used in the preparation of Figures 9 and 10 in which $\sim 30\%$ of the aerosol optical thickness at 765 nm was above the boundary layer. The resulting corrections at the scan center using M50 as the base profile are provided in Figure 11. Comparing Figures 9a with 11a, 9b with 11b, 10a with 11c, and 10b with 11d, we see that the filled circles are $\lesssim 0.001$ (and typically much less) lower using the M50 base profile compared to the M80-T50-B base profile. Thus, a large error in the base profile does not significantly influence the overall atmospheric correction. In fact, for the $VR = 15$ km case, the incorrect base profile actually produces better corrections. Similar results are obtained at the scan edge (not shown).

Volcanic Aerosols

A situation in which the base profile can strongly influence the atmospheric correction is that following volcanic eruptions, e.g., El Chichón, which can inject significant quantities of aerosol into the stratosphere. To understand the effect of this on the O_2 correction presented above, we have

examined four cases with volcanic aerosol. We used the El Chichón aerosol model developed by King et al.²⁰ and considered the aerosol to be concentrated in a layer from 18 to 20 km (Figure 2). The optical thickness at 550 nm was taken to be 0.05 or 0.10. Figure 12 provides the results of simulated retrieval errors $\Delta\rho$ at the scan center as a function of θ_0 . The notation for the aerosol profile now includes “V” followed by a number indicating the volcanic aerosol optical thickness at 550 nm, e.g., M80-T50-B-V05 indicates the addition of a volcanic aerosol with optical thickness 0.05 at 550 nm, etc. Examination of Figure 12 shows that the error in the presence of the O_2 absorption (filled circles) is always below (more negative) the error what would occur in the absence of O_2 absorption (open circles). This occurs because the presence of the volcanic aerosol causes less O_2 absorption than the base profile. Thus, $P_A(M)$ in Eq. (6) is too large so ρ_A will be too large resulting in an overcorrection ($\Delta\rho < 0$). The effect is more significant the greater the contribution from the volcanic aerosol compared to the boundary-layer aerosol. This can be seen by comparing Figures 9a, 12a, and 12b for which the volcanic optical thickness progresses from 0 to 0.05 to 0.10 with $VR = 40$ km, and Figures 10a, 12c, and 12d, for $VR = 15$ km. For $VR = 40$ km, we see a slow degradation in the quality of the atmospheric correction even in the absence of O_2 absorption with increasing volcanic optical thickness and a large overcorrection in the presence of O_2 absorption. In contrast, for $VR = 15$ km we see the same slow degradation in the absence of O_2 absorption, but a smaller O_2 absorption overcorrection.

It is clear that application of the proposed O_2 absorption correction in the presence of volcanic aerosol will require information concerning the vertical distribution, concentration, and optical properties of the volcanic aerosol.

Summary and Conclusions

By simulating the radiance reflected from the ocean-atmosphere system in the O_2 “A” absorption band using a line-by-line backward Monte Carlo radiative transfer code, we have shown the influence of the absorption band on the atmospheric correction of ocean color sensors utilizing a $\sim 745\text{--}785$ spectral band, e.g., SeaWiFS and OCTS. If the O_2 absorption is ignored, unacceptable errors in the water-leaving reflectance will result (Table 5). However, given an aerosol profile — the base profile — through simulations we have found a simple empirical relationship (Eq. (6))

that removes the effect of the absorption from the aerosol component of the reflectance ($\rho_a + \rho_{ra}$). Combining this with a similar empirical expression (Eq. (4)) for the Rayleigh scattering component (ρ_r), allows application of the atmospheric correction algorithm developed by Gordon and Wang,⁹ that ignored the O₂ absorption. Test simulations in which the actual aerosol profile and the base profiles were identical *above* the marine boundary layer suggest that the difference in the error in the retrieval of the water-leaving reflectance due to the presence of the O₂ absorption is usually reduced to $\ll 0.001$ using the empirical relations. An important feature of this method of correction for the effects of the O₂ absorption is that it employs lookup tables that can be prepared in the absence of O₂ absorption using more efficient radiative transfer codes.

The dependence of the O₂ absorption correction on an assumed profile is unsatisfying; however, the dependence is very weak (Figures 6, 7, and 11). One exception is the addition of volcanic aerosol which, if ejected into the stratosphere, will cause serious difficulty in the removal of the O₂ absorption effect (Figure 12). A second exception is the presence of thin cirrus clouds. These will produce effects similar to volcanic aerosols. However, in either case the atmospheric correction even in the absence of O₂ absorption is seen to be degraded by the introduction of a high-altitude aerosol layer (e.g., compare Figures 10a, 12c, and 12d). Recalling that in the Gordon and Wang⁹ correction algorithm it was assumed that *all* of the aerosol is in the marine boundary layer, this suggests that the basic algorithm itself may have to be modified to incorporate the effects of such aerosols. A simple modification would be to use a more realistic vertical distribution of aerosol which would include some aerosol in the free troposphere and stratosphere. This would also improve the performance of the algorithm in the presence of O₂ absorption.

Finally, it may be possible to identify the presence of volcanic aerosol or cirrus clouds from SeaWiFS imagery. A method we are examining involves the SeaWiFS band at 670 nm. For $C \lesssim 1$ mg/m³, ρ_w at 670 nm is very small, i.e., $\lesssim 0.0008$. Simulations at 670 nm with volcanic aerosol (similar to those presented in Figure 12) suggest that the recovered ρ_w there will be negative if there is a significant volcanic aerosol layer, e.g., a stratospheric aerosol optical thickness of 0.05 – 0.10. Thin cirrus clouds would produce a similar effect.

References

- [1] W. A. Hovis, D. K. Clark, F. Anderson, R. W. Austin, W. H. Wilson, E. T. Baker, D. Ball, H. R. Gordon, J. L. Mueller, S. Y. E. Sayed, B. Strum, R. C. Wrigley and C. S. Yentsch, "Nimbus 7 coastal zone color scanner: system description and initial imagery," *Science* **210**, 60–63 (1980).
- [2] H. R. Gordon, D. K. Clark, J. L. Mueller and W. A. Hovis, "Phytoplankton pigments derived from the Nimbus-7 CZCS: initial comparisons with surface measurements," *Science* **210**, 63–66 (1980).
- [3] H. R. Gordon, J. W. Brown and R. H. Evans, "Exact Rayleigh Scattering Calculations for use with the Nimbus-7 Coastal Zone Color Scanner," *Applied Optics* **27**, 862–871 (1988).
- [4] H. R. Gordon and D. K. Clark, "Clear water radiances for atmospheric correction of coastal zone color scanner imagery," *Applied Optics* **20**, 4175–4180 (1981).
- [5] G. C. Feldman, N. Kuring, C. Ng, W. Esaias, C. R. McClain, J. Elrod, N. Maynard, D. Endres, R. Evans, J. Brown, S. Walsh, M. Carle and G. Podesta, "Ocean Color: Availability of the Global Data Set," *EOS Trans. Amer. Geophys. Union* **70**, 634–641 (1989).
- [6] R. H. Evans and H. R. Gordon, "CZCS 'System Calibration:' A retrospective examination," *Jour. Geophys. Res.* **99C**, 7293–7307 (1994).
- [7] S. B. Hooker, W. E. Esaias, G. C. Feldman, W. W. Gregg and C. R. McClain, *SeaWiFS Technical Report Series: Volume 1, An Overview of SeaWiFS and Ocean Color* (NASA Technical Memorandum 104566, July 1992).

- [8] V. V. Salomonson, W. L. Barnes, P. W. Maymon, H. E. Montgomery and H. Ostrow, "MODIS: Advanced Facility Instrument for Studies of the Earth as a System," *IEEE Geosci. Rem. Sens.* **27**, 145–152 (1989).
- [9] H. R. Gordon and M. Wang, "Retrieval of water-leaving radiance and aerosol optical thickness over the oceans with SeaWiFS: A preliminary algorithm," *Applied Optics* **33**, 443–452 (1994).
- [10] P. Y. Deschamps, M. Herman and D. Tanre, "Modeling of the atmospheric effects and its application to the remote sensing of ocean color," *Applied Optics* **22**, 3751–3758 (1983).
- [11] H. R. Gordon, D. K. Clark, J. W. Brown, O. B. Brown, R. H. Evans and W. W. Broenkow, "Phytoplankton pigment concentrations in the Middle Atlantic Bight: comparison between ship determinations and Coastal Zone Color Scanner estimates," *Applied Optics* **22**, 20–36 (1983).
- [12] M. Wang and H. R. Gordon, "*Influence of Oceanic Whitecaps on Atmospheric Correction of SeaWiFS*," Accepted for publication in *Applied Optics*.
- [13] W. M. Balch, P. M. Holligan, S. G. Ackleson and K. J. Voss, "Biological and optical properties of mesoscale coccolithophore blooms in the Gulf of Maine," *Limnology and Oceanography* **34**, 629–643 (1991).
- [14] E. P. Shettle and R. W. Fenn, *Models for the Aerosols of the Lower Atmosphere and the Effects of Humidity Variations on Their Optical Properties* (Air Force Geophysics Laboratory, Hanscomb AFB, MA 01731, AFGL-TR-79-0214, 1979).
- [15] L. S. Rothman, R. R. Gamache, A. Barbe, A. Goldman, J. R. Gillis, L. R. Brown, R. A. Toth, J. -M. Flaud and C. Camy-Peyret, "AFGL atmospheric absorption line parameters compilation: 1982 edition," *Applied Optics* **22**, 2247–2256 (1983).

- [16] R. W. Fenn, S. A. Clough, W. O. Gallery, R. E. Good, F. X. Kenizys, J. D. Mill, L. S. Rothman, E. P. Shettle and F. E. Volz, "Optical and Infrared Properties of the Atmosphere," in *Handbook of Geophysics and the Space Environment*, edited by A. S. Jursa (Air Force Geophysics Laboratory, Hanscomb AFB, MA, 1985) p. 18-1-18-80.
- [17] C. Cox and W. Munk, "Measurements of the Roughness of the Sea Surface from Photographs of the Sun's Glitter," *Jour. Opt. Soc. of Am.* **44**, 838-850 (1954).
- [18] COESA, "*U.S. Standard Atmosphere 1976*," U.S. Government Printing Office, Washington, D.C. 1976.
- [19] WCP-112, *A preliminary cloudless standard atmosphere for radiation computation* (World Meteorological Organization, WMO/TD-No. 24, Geneva).
- [20] M. D. King, Harshvardhan and A. Arking, "A Model of the Radiative Properties of the El Chichón Stratospheric Aerosol Layer," *Journal of Climate and Applied Meteorology* **23**, 1121-1137 (1984).
- [21] F. X. Kenizys, E. P. Shettle, L. W. Abreu, G. P. Anderson, J.H.Chetwynd, W. O. Gallery, J. E. A. Selby and S. A. Clough, *Atmospheric Transmittance/Radiance: The LOWTRAN 7 Model* (Air Force Geophysics Laboratory, Hanscomb AFB, MA 01731, 1989), In Preparation.
- [22] R. G. Isaacs, W. -C. Wang, R. D. Worsham and S. Goldenberg, "Multiple scattering LOW-TRAN and FASCODE models," *Applied Optics* **28**, 1272-1281 (1987).
- [23] K. N. Liou, *Radiation and Cloud Processes in the Atmosphere* (Oxford University Press, New York, 1992), 487 pp.

- [24] W. A. Hoppel, J. W. Fitzgerald, G. M. Frick, R. E. Larson and E. J. Mack, "Aerosol Size Distributions and Optical Properties Found in the Marine Boundary Layer Over the Atlantic Ocean," *J. Geophys Res.* **95D**, 3659–3686 (1990).

- [25] P. J. Reddy, F. W. Kreiner, J. J. Deluisi and Y. Kim, "Aerosol Optical Depths Over the Atlantic Derived From Shipboard Sunphotometer Observations During the 1988 Global Change Expedition," *Global Biogeochemical Cycles* **4**, 225–240 (1990).

Figure Captions

Figure 1. A portion of the O₂ A band at 762 nm covering approximately 1.165 nm.

Figure 2. Schematic of the aerosol profile for the atmospheric model described in the text.

Figure 3. Fractional change in reflectance $(\rho_r - \rho'_r)/\rho'_r$, as a function of M for a spectral band from 745 to 785 nm.

Figure 5. Fractional change in reflectance $(\rho_A - \rho'_A)/\rho'_A$, as a function of M for a spectral band from 745 to 785 nm.

Figure 6. Error in the prediction of ρ_A from ρ'_A when the actual aerosol profile differs from the base profile. h is the aerosol scale height. All test profiles use M50.

Figure 7. Error in the prediction of ρ_A from ρ'_A when the actual aerosol profile differs from the base profile. h is the aerosol scale height. All test profiles use T50.

Figure 8. $(\rho_A - \rho'_A)/\rho'_A$ as a function of M for the selected base profile.

Figure 9a. Error in the retrieved $t(443)\rho_w(443)$ for viewing at the center of the scan with aerosol profile M80-T50-B and $VR = 40$ km.

Figure 9b. Error in the retrieved $t(443)\rho_w(443)$ for viewing at the center of the scan with aerosol profile T80-T50-B and $VR = 40$ km.

Figure 9c. Error in the retrieved $t(443)\rho_w(443)$ for viewing at the edge of the scan with aerosol profile M80-T50-B and $VR = 40$ km.

Figure 9d. Error in the retrieved $t(443)\rho_w(443)$ for viewing at the edge of the scan with aerosol profile T80-T50-B and $VR = 40$ km.

Figure 10a. Error in the retrieved $t(443)\rho_w(443)$ for viewing at the center of the scan with aerosol profile M80-T50-B and $VR = 15$ km.

Figure 10b. Error in the retrieved $t(443)\rho_w(443)$ for viewing at the center of the scan with aerosol profile T80-T50-B and $VR = 15$ km.

Figure 10c. Error in the retrieved $t(443)\rho_w(443)$ for viewing at the edge of the scan with aerosol profile M80-T50-B and $VR = 15$ km.

Figure 10d. Error in the retrieved $t(443)\rho_w(443)$ for viewing at the edge of the scan with aerosol profile T80-T50-B and $VR = 15$ km.

Figure 11a. Error in the retrieved $t(443)\rho_w(443)$ for viewing at the center of the scan with aerosol profile M80-T50-B and $VR = 40$ km, and a simplified base profile.

Figure 11b. Error in the retrieved $t(443)\rho_w(443)$ for viewing at the center of the scan with aerosol profile T80-T50-B and $VR = 40$ km, and a simplified base profile.

Figure 11c. Error in the retrieved $t(443)\rho_w(443)$ for viewing at the center of the scan with aerosol profile M80-T50-B and $VR = 15$ km, and a simplified base profile.

Figure 11d. Error in the retrieved $t(443)\rho_w(443)$ for viewing at the center of the scan with aerosol profile T80-T50-B and $VR = 40$ km, and a simplified base profile.

Figure 12a. Error in the retrieved $t(443)\rho_w(443)$ for viewing at the center of the scan with aerosol profile M80-T50-B and $VR = 40$ km, and the standard base profile, when Volcanic aerosol (V) is added with optical thickness 0.05 at 550 nm.

Figure 12b. Error in the retrieved $t(443)\rho_w(443)$ for viewing at the center of the scan with aerosol profile M80-T50-B and $VR = 40$ km, and the standard base profile, when Volcanic aerosol (V) is added with optical thickness 0.10 at 550 nm.

Figure 12c. Error in the retrieved $t(443)\rho_w(443)$ for viewing at the center of the scan with aerosol profile M80-T50-B and $VR = 15$ km, and the standard base profile, when Volcanic aerosol (V) is added with optical thickness 0.05 at 550 nm.

Figure 12d. Error in the retrieved $t(443)\rho_w(443)$ for viewing at the center of the scan with aerosol profile M80-T50-B and $VR = 15$ km, and the standard base profile, when Volcanic aerosol (V) is added with optical thickness 0.10 at 550 nm.

Table 1: Total aerosol optical thickness for model M80-T50-B

VR (km)	λ (nm)			
	443	550	765	865
15	0.7029	0.6345	0.5509	0.5334
40	0.3594	0.3085	0.2462	0.2259

Table 2: Boundary-layer aerosol optical thickness for model M80-T50-B

VR (km)	λ (nm)			
	443	550	765	865
15	0.5242	0.4974	0.4648	0.4538
40	0.1806	0.1738	0.1602	0.1563

Table 3: Total aerosol optical thickness for model T80-T50-B

VR (km)	λ (nm)			
	443	550	765	865
15	0.8226	0.6345	0.4037	0.3289
40	0.4006	0.3085	0.1955	0.1589

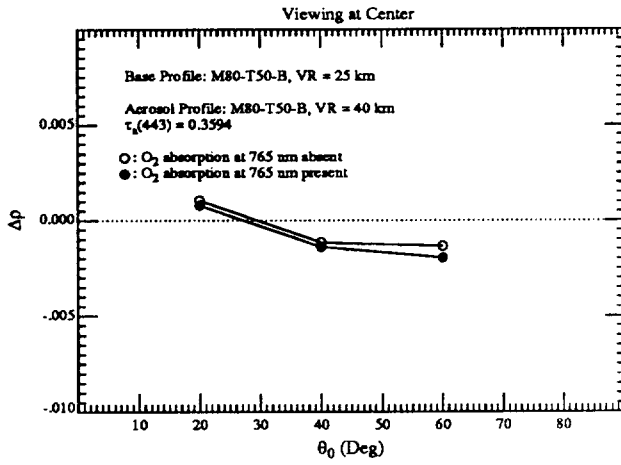
Table 4: Boundary-layer aerosol optical thickness for model T80-T50-B

VR (km)	λ (nm)			
	443	550	765	865
15	0.6438	0.4974	0.3176	0.2592
40	0.2218	0.1738	0.1095	0.0893

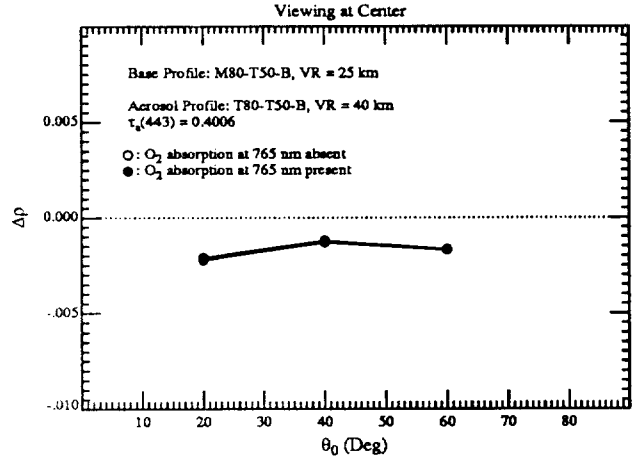
Table 5: $\Delta\rho$ when existence of O_2 absorption is ignored.

Model	VR (km)	Scan Center	Scan Edge	
M80-T50-B	40	~ 0.012	~ 0.014	
M80-T50-B	15	~ 0.013	~ 0.016	
T80-T50-B	40	~ 0.028	~ 0.020	
T80-T50-B	15	~ 0.029	~ 0.031	

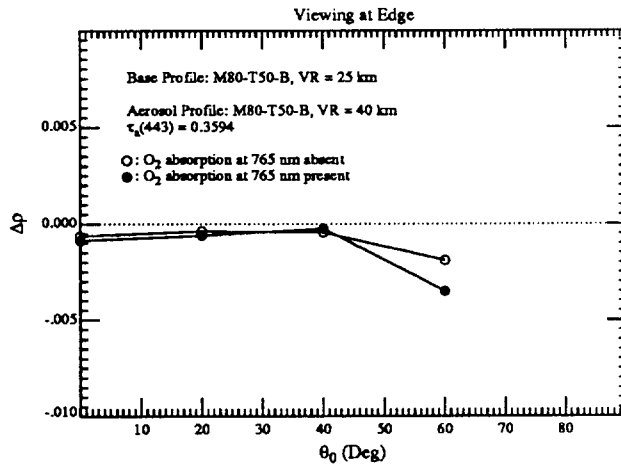
Suggested layout for Figure 9



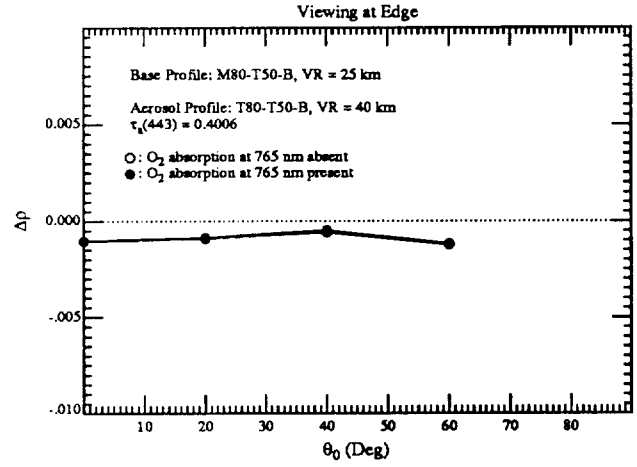
(a)



(b)

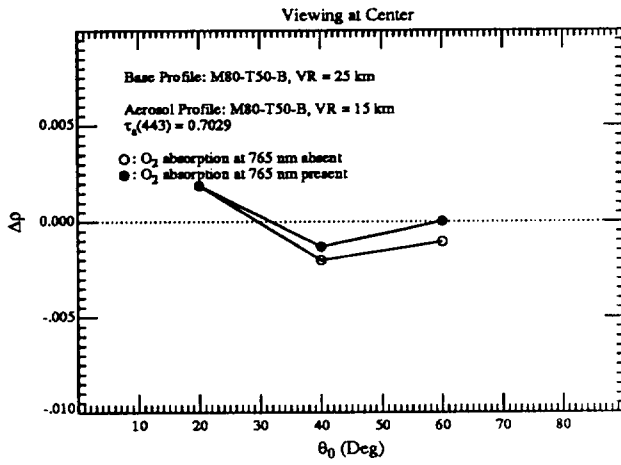


(c)

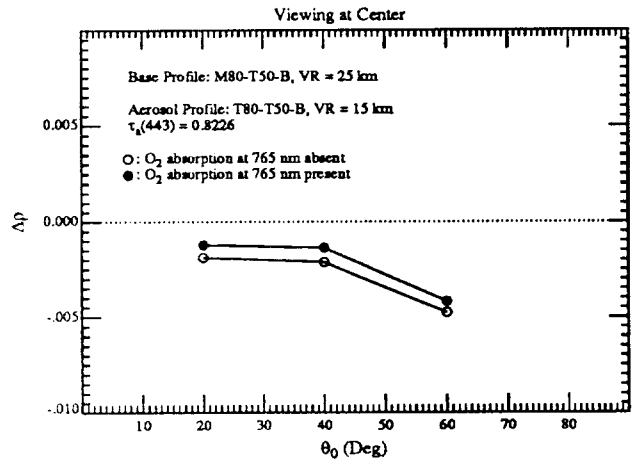


(d)

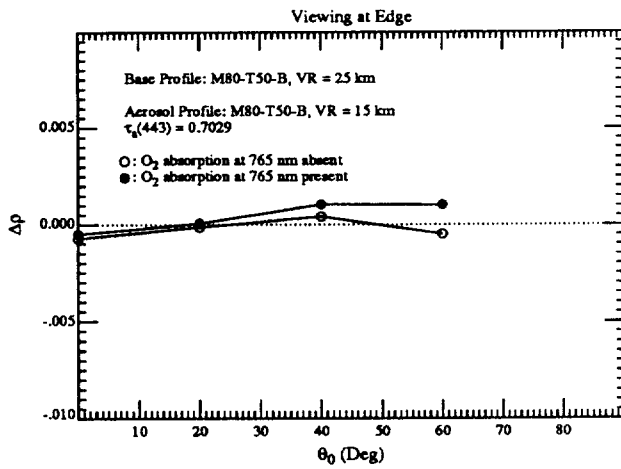
Suggested layout for Figure 10



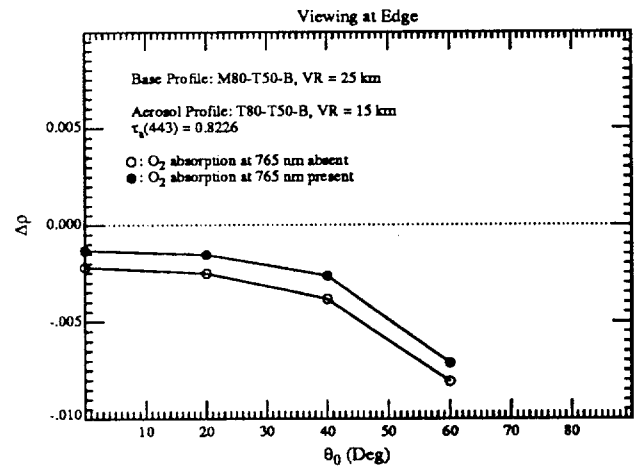
(a)



(b)

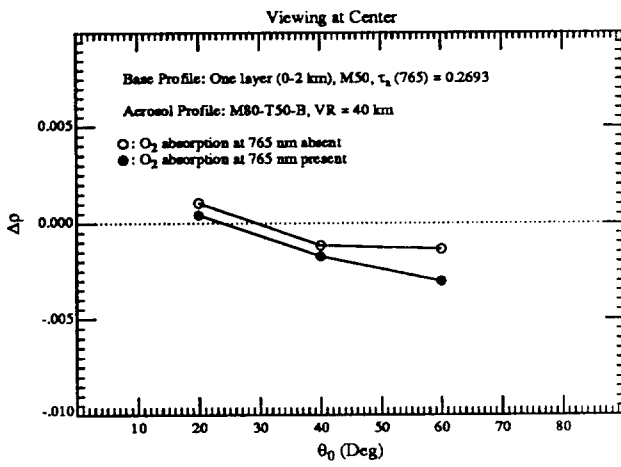


(c)

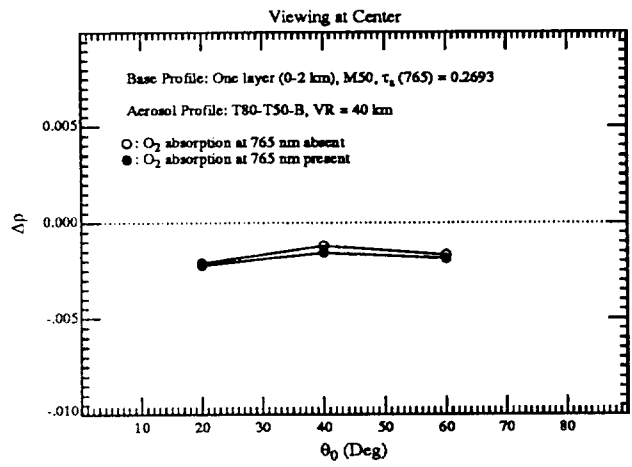


(d)

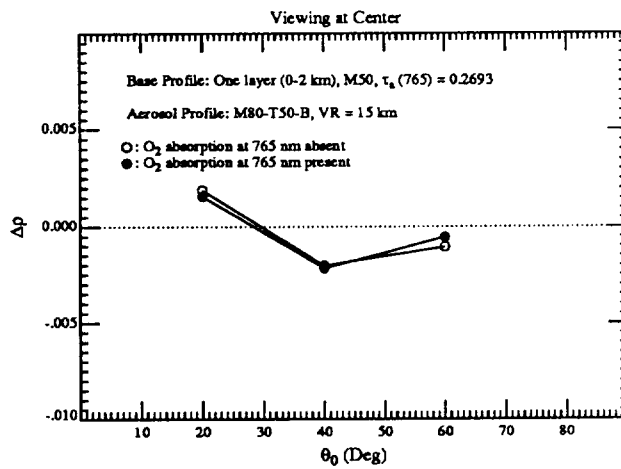
Suggested layout for Figure 11



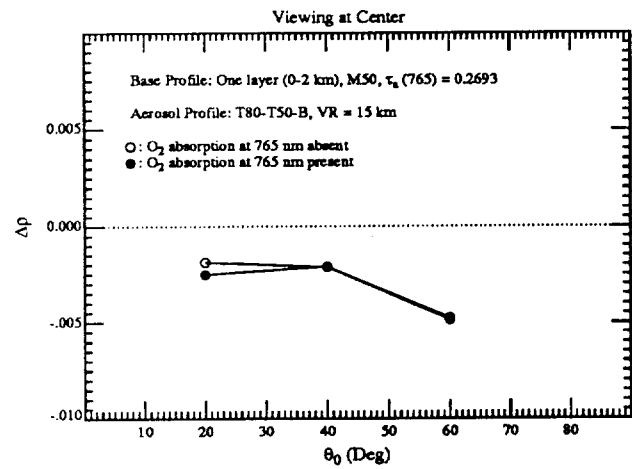
(a)



(b)

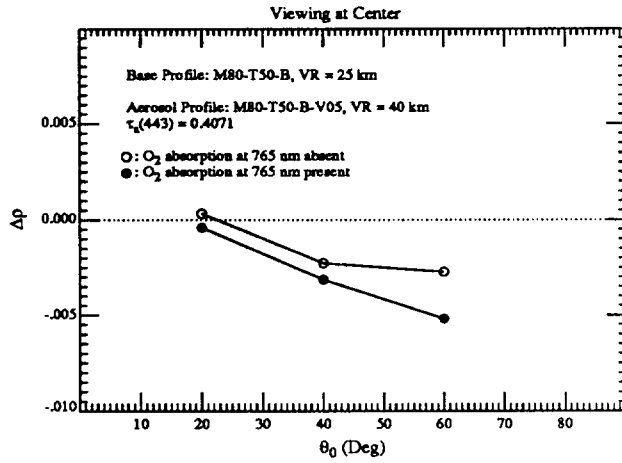


(c)

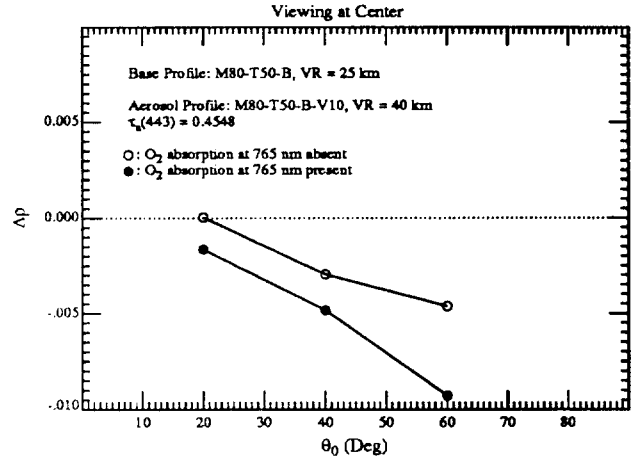


(d)

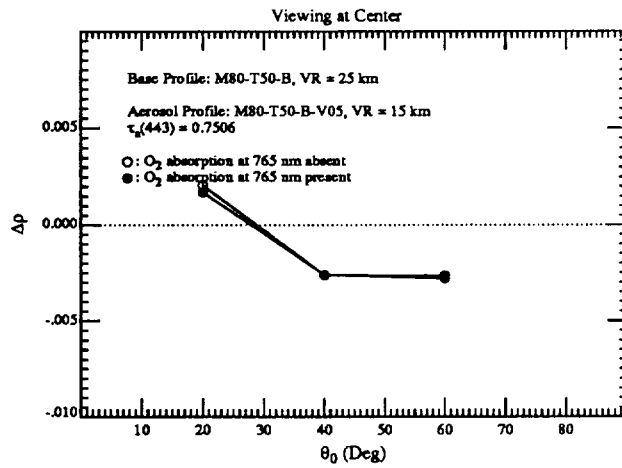
Suggested layout for Figure 12



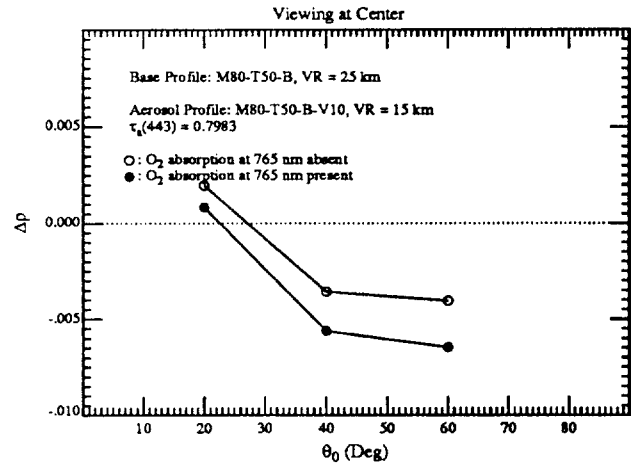
(a)



(b)



(c)



(d)

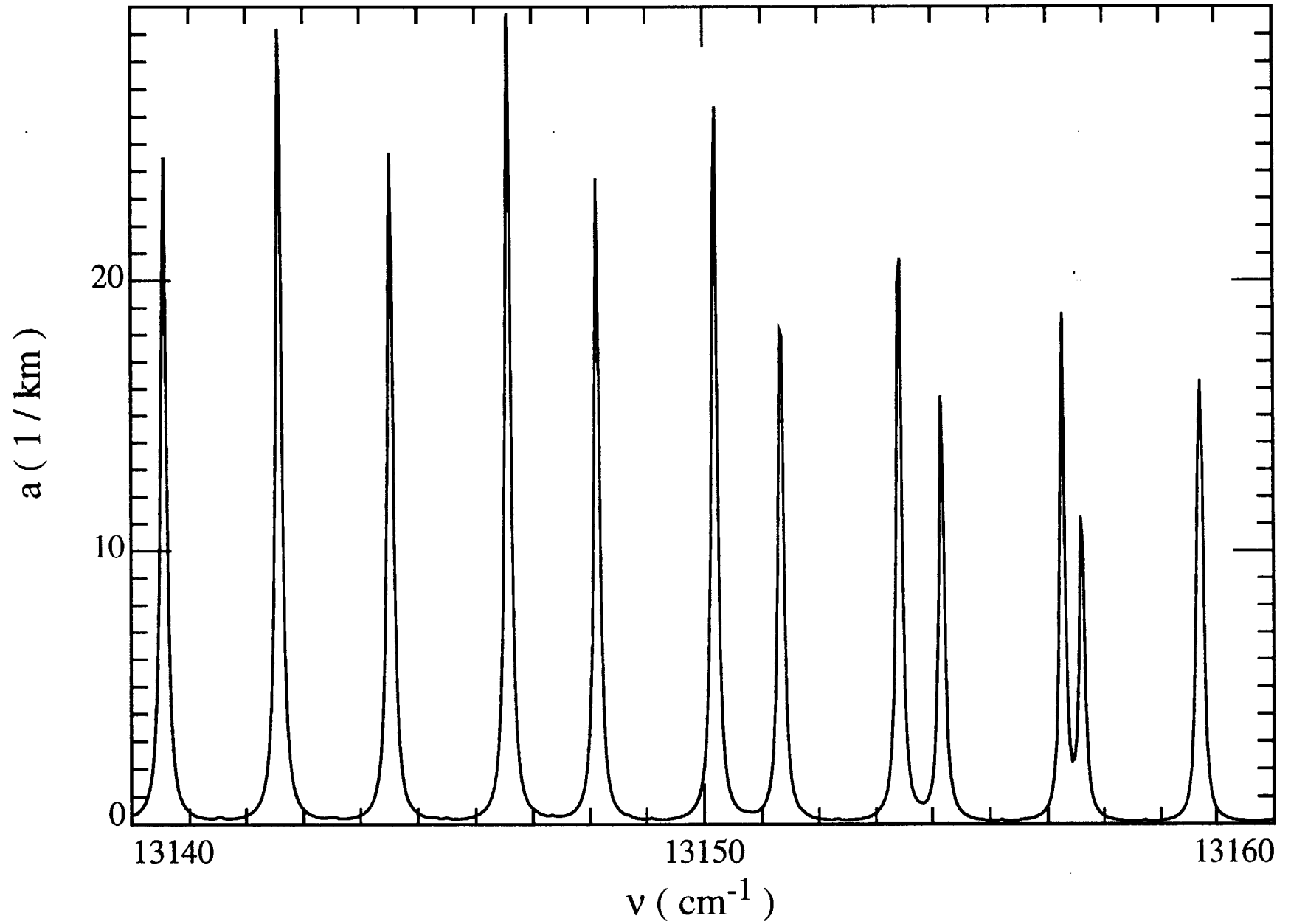


Fig 1

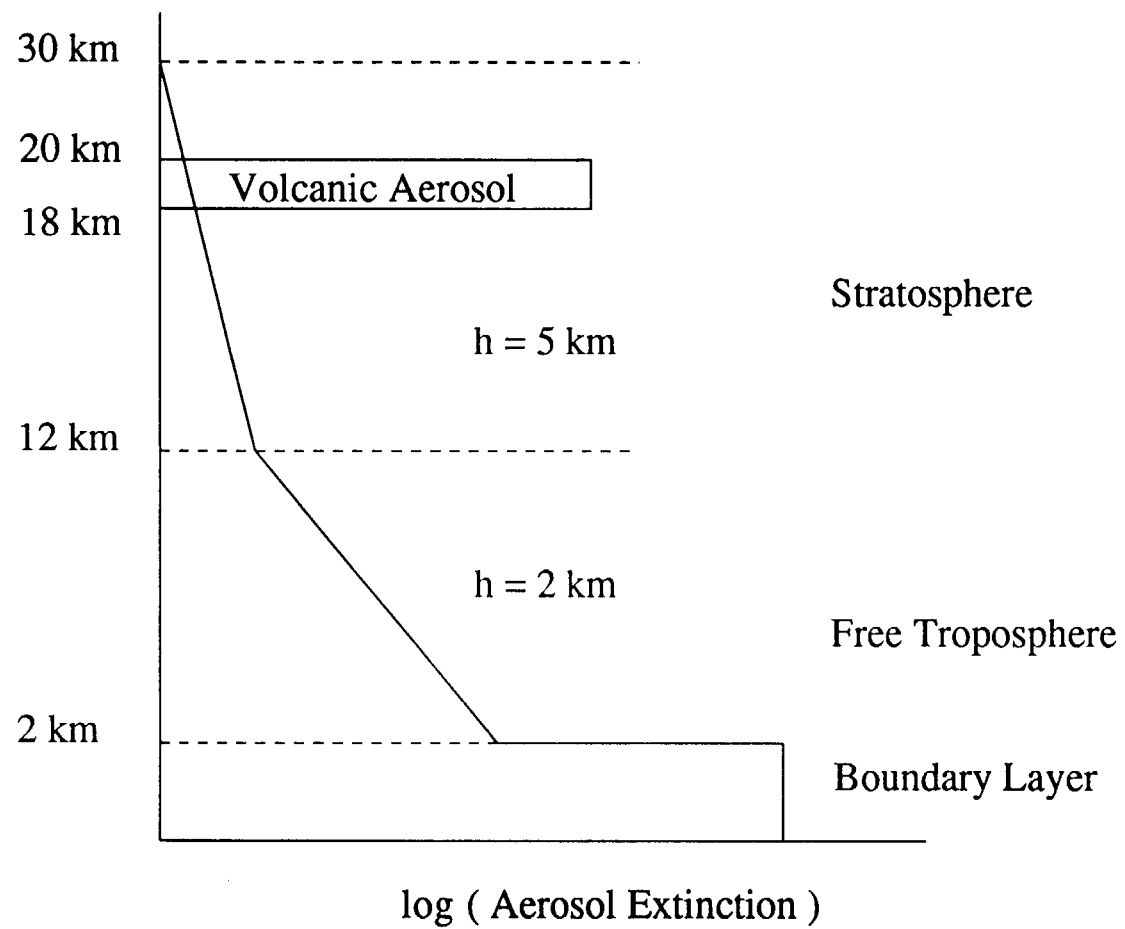


Fig. 2

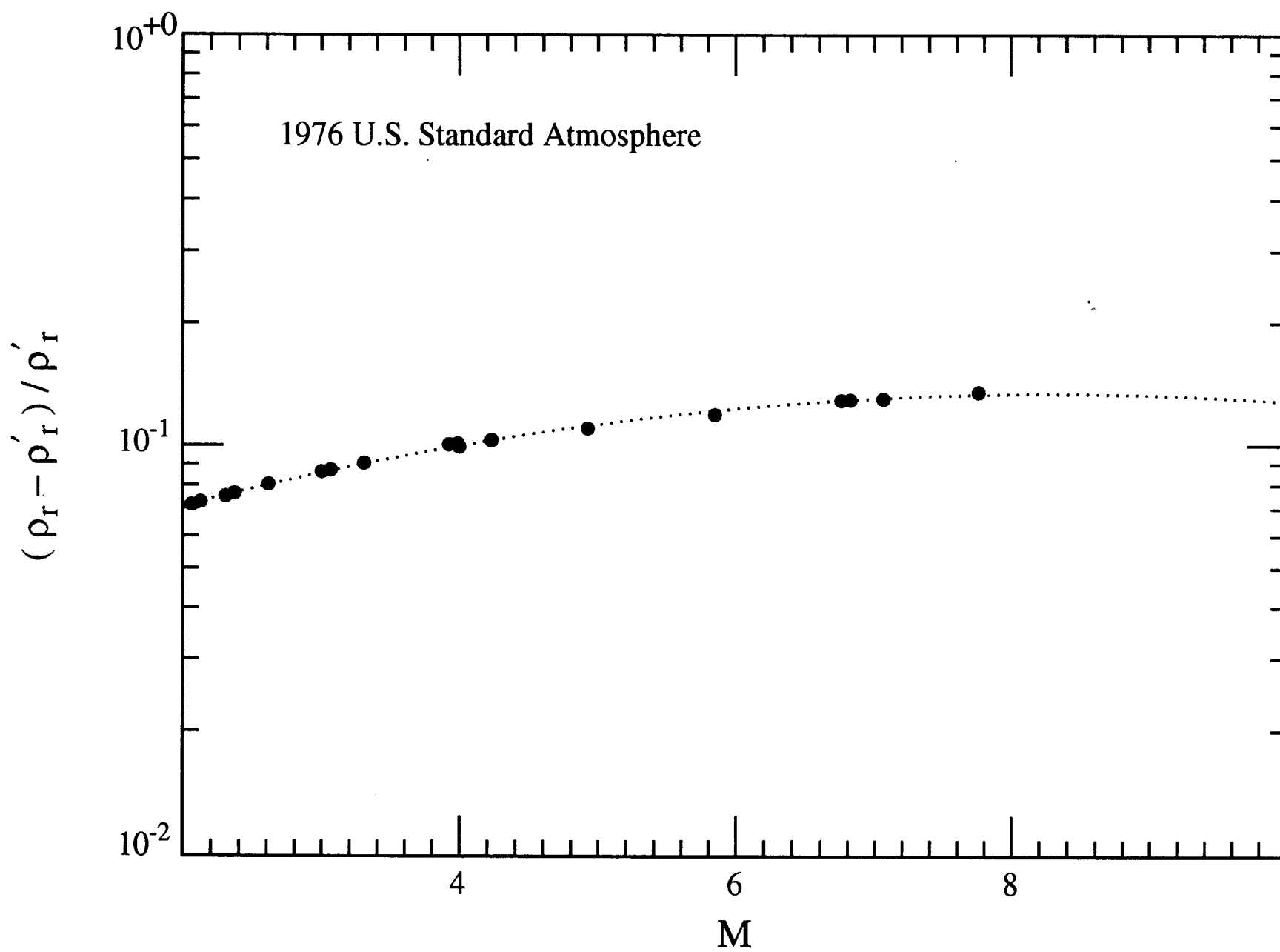


Fig. 3

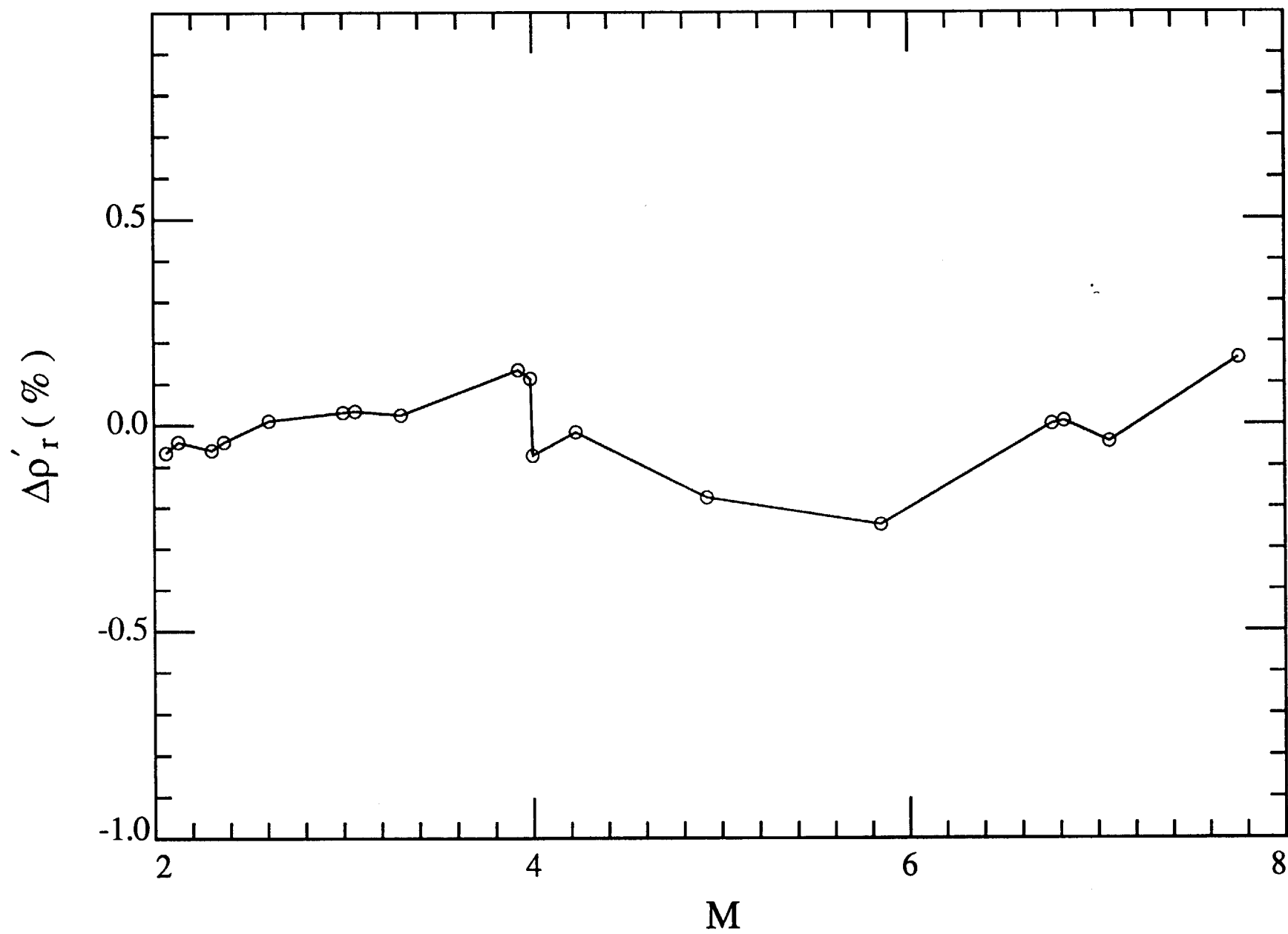


Fig. 4

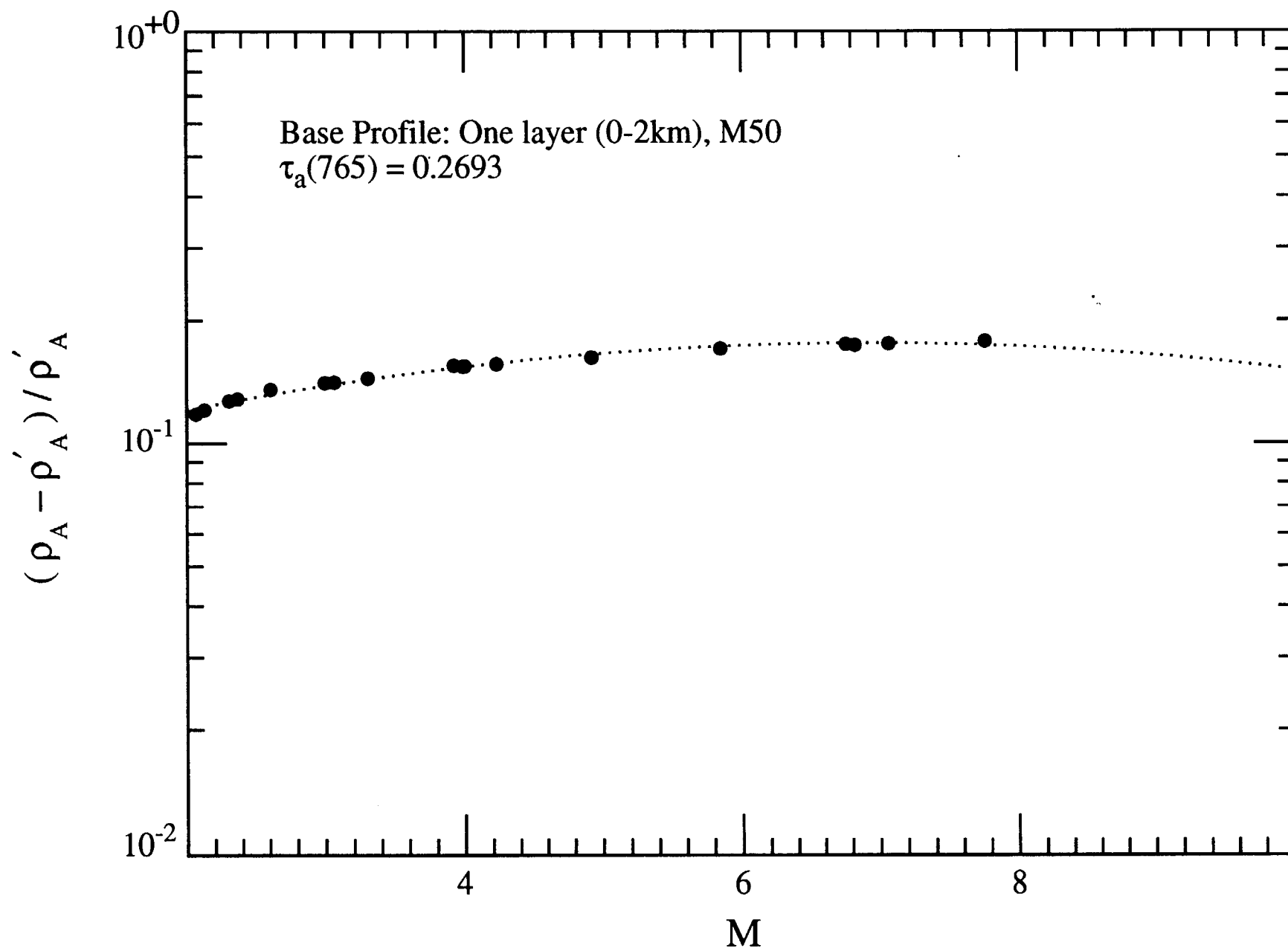


Fig. 5

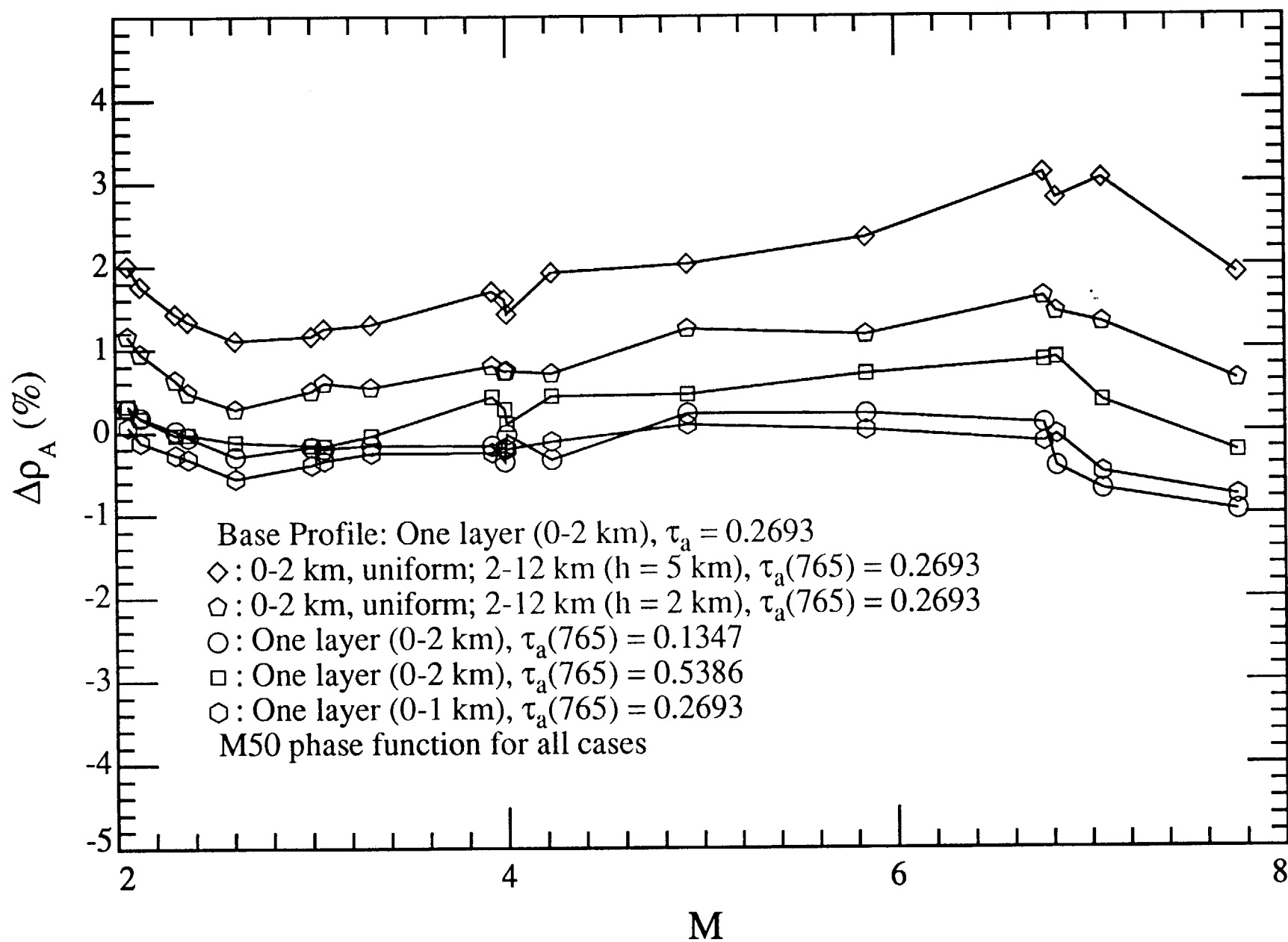


Fig. 6

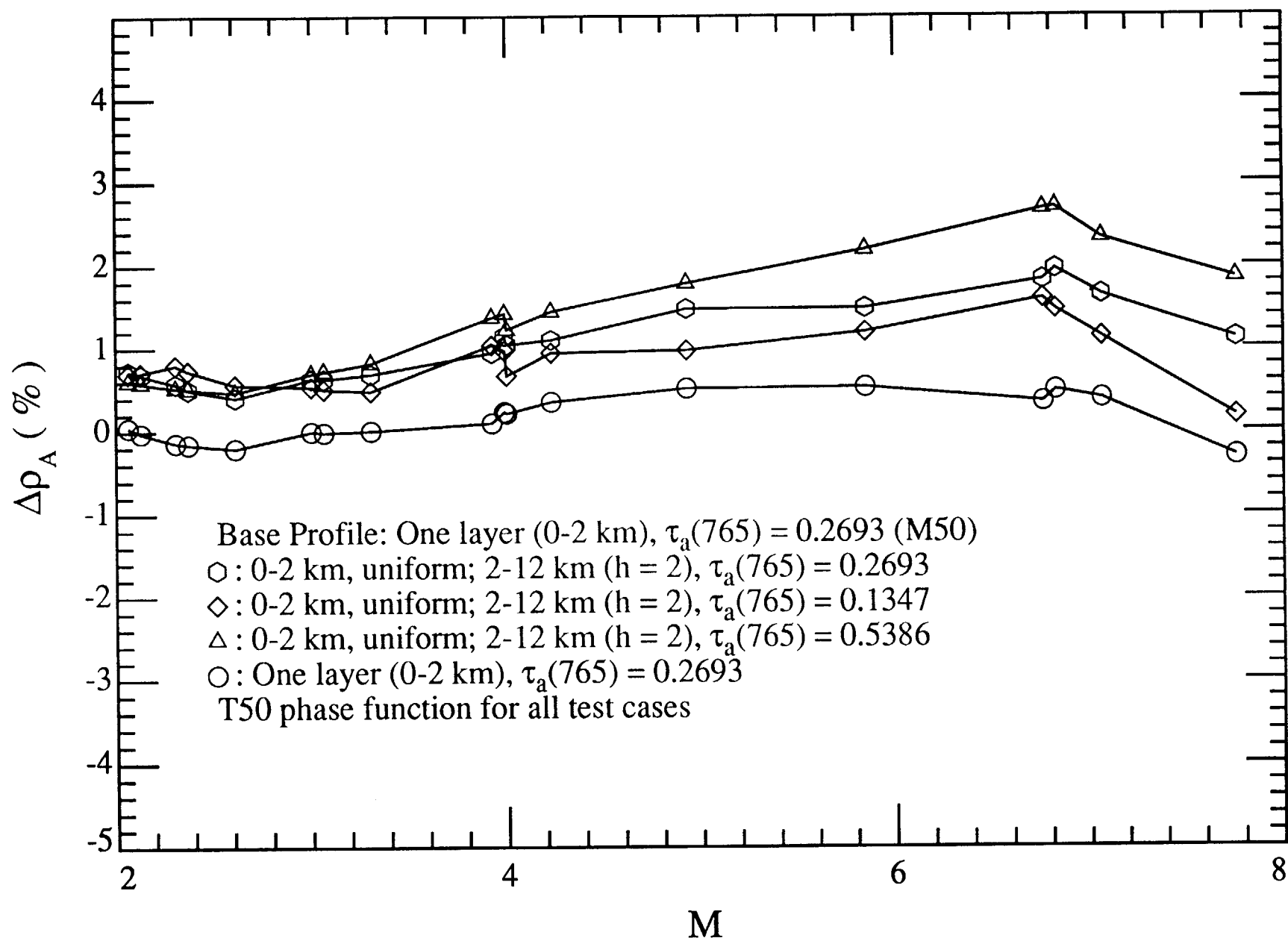


Fig. 7

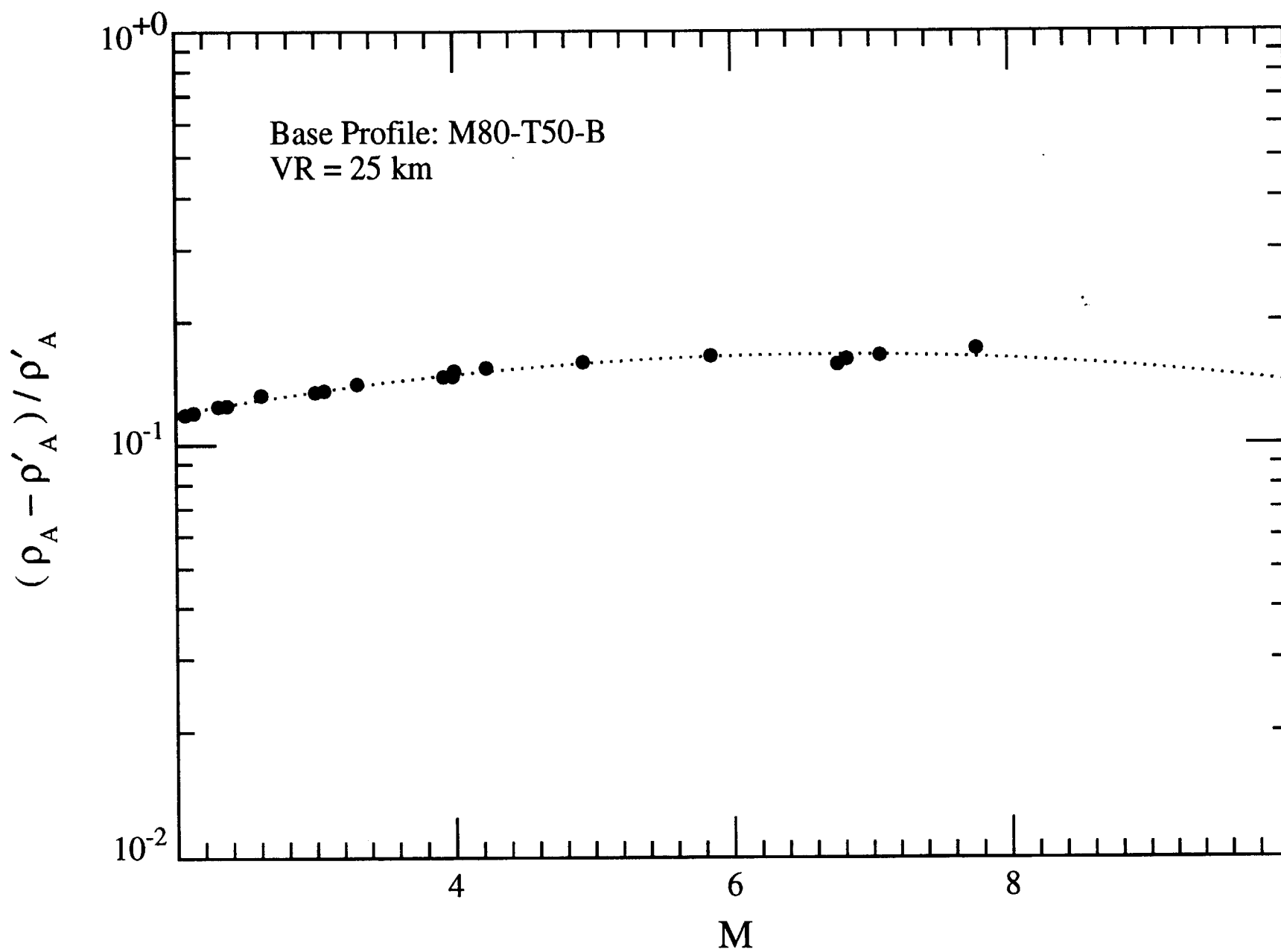


Fig. 8

Viewing at Center

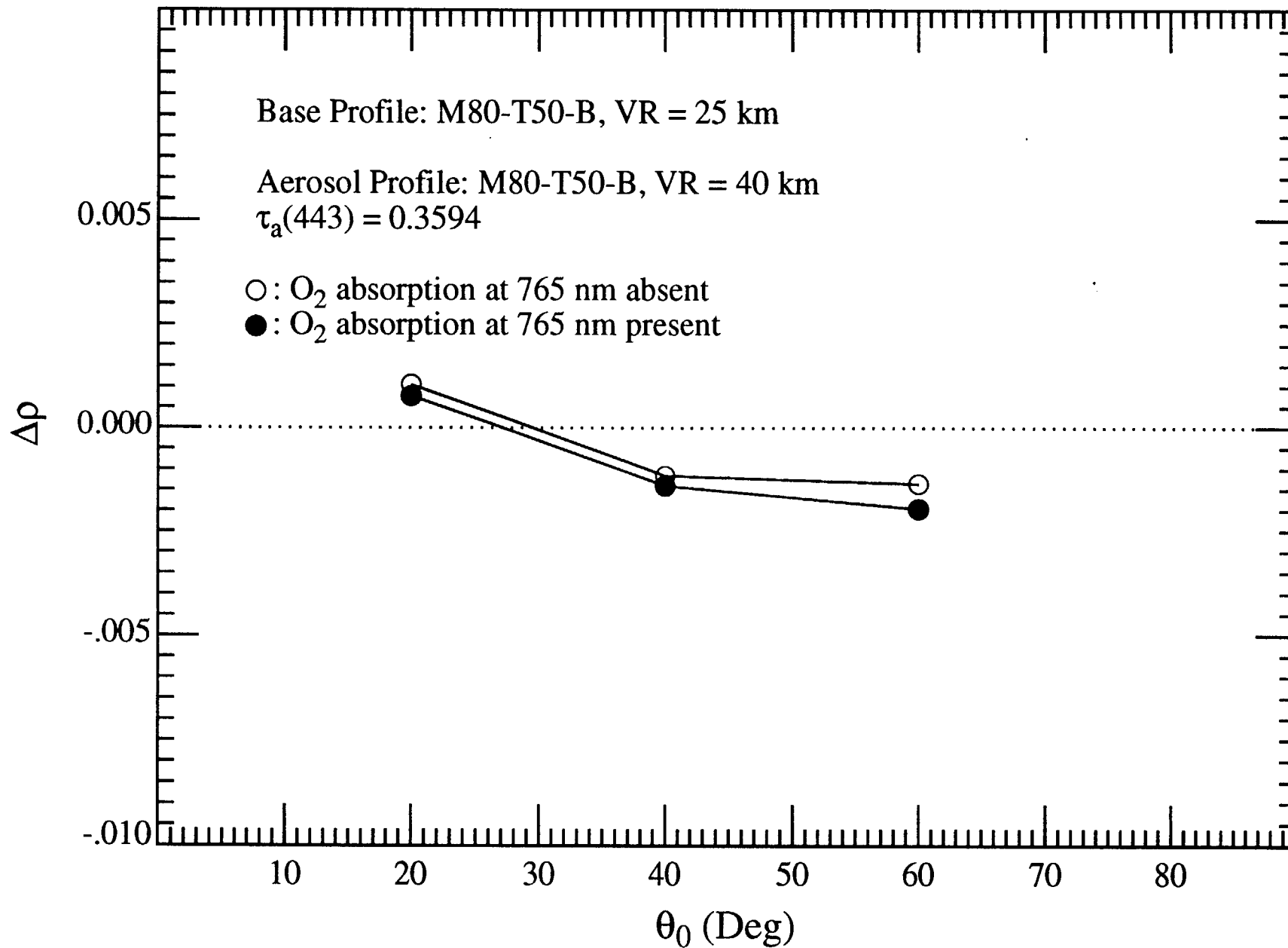


Fig. 9a

Viewing at Center

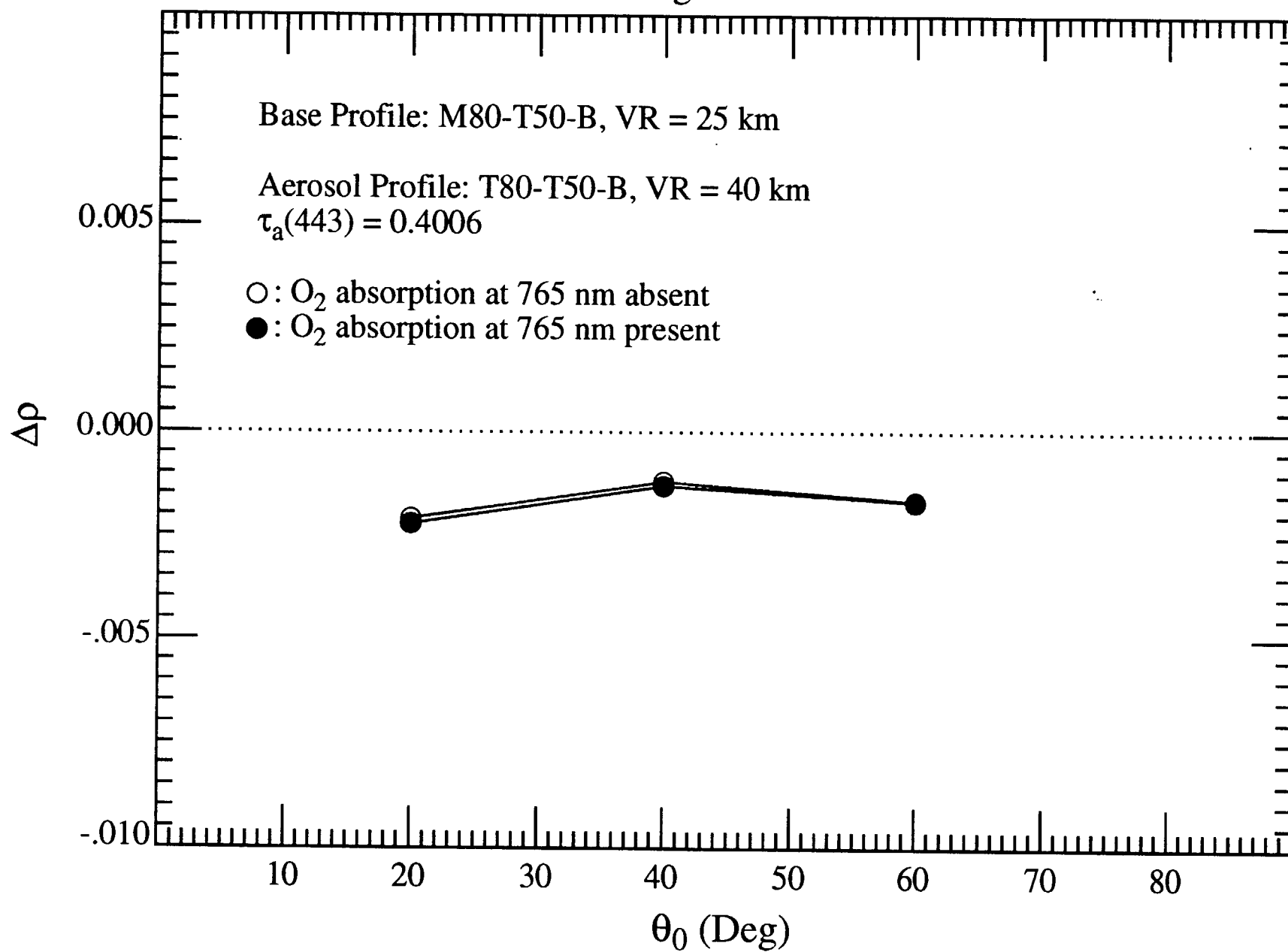


Fig 9b

Viewing at Edge

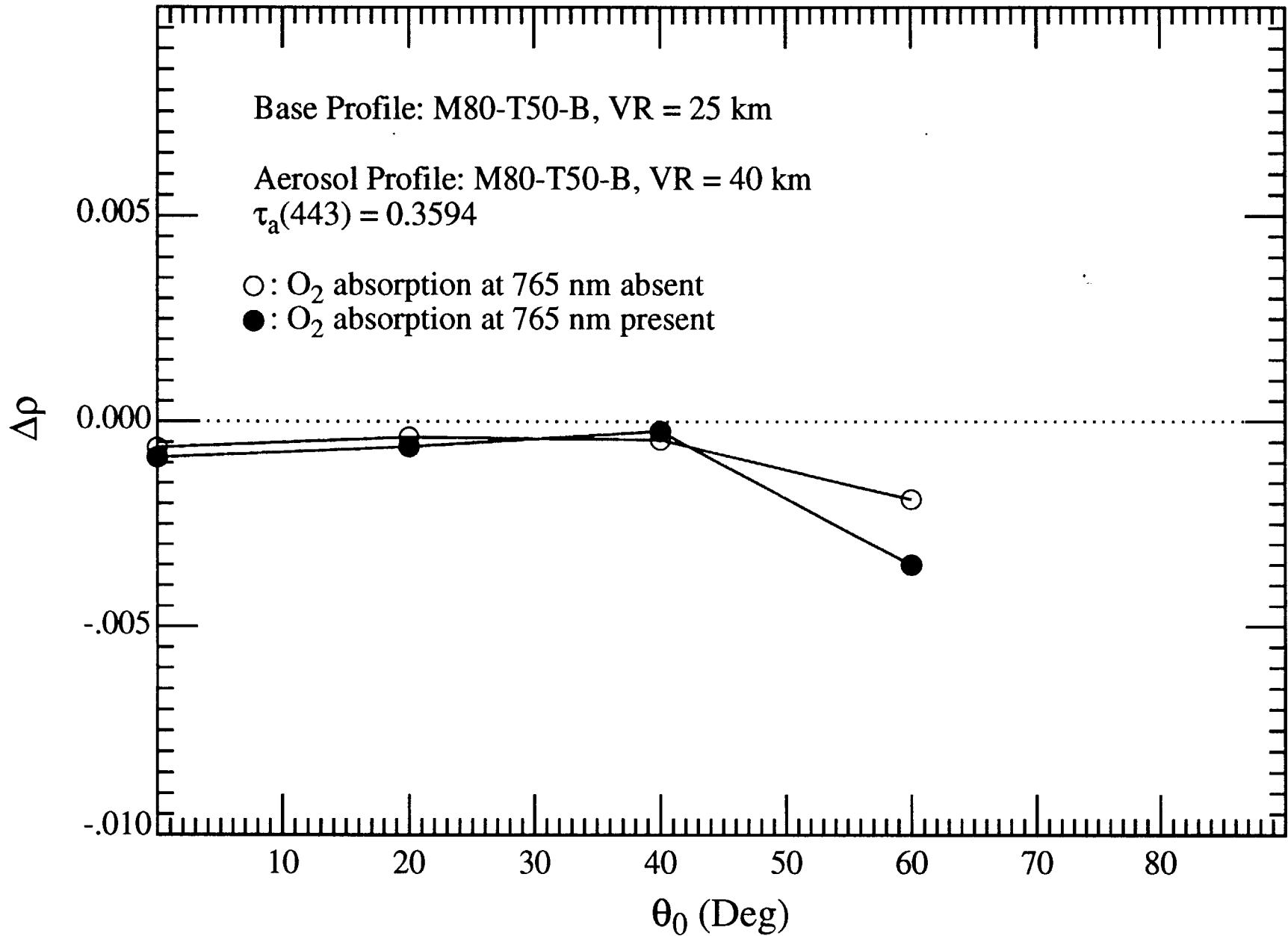


Fig. 9c

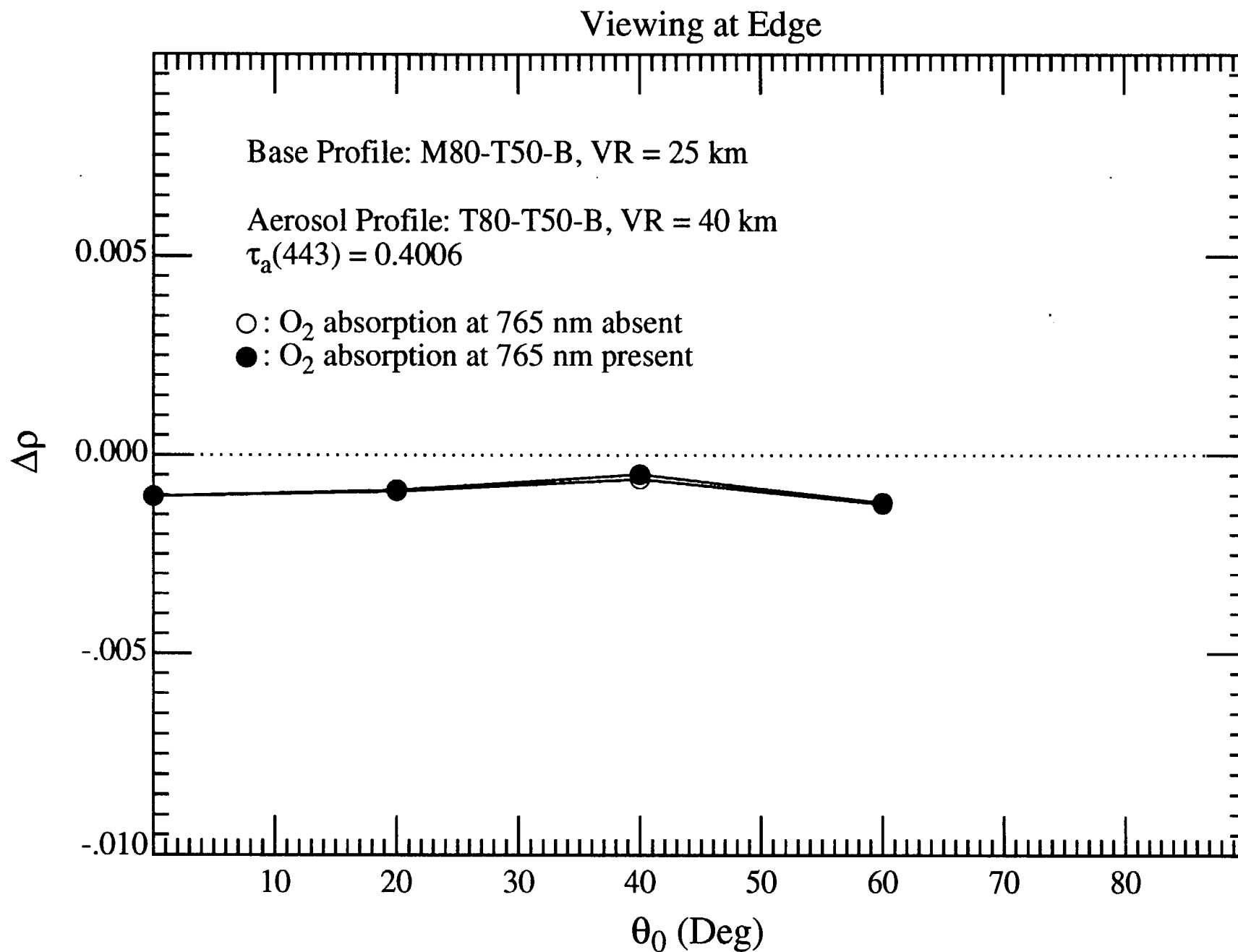


Fig. 9d

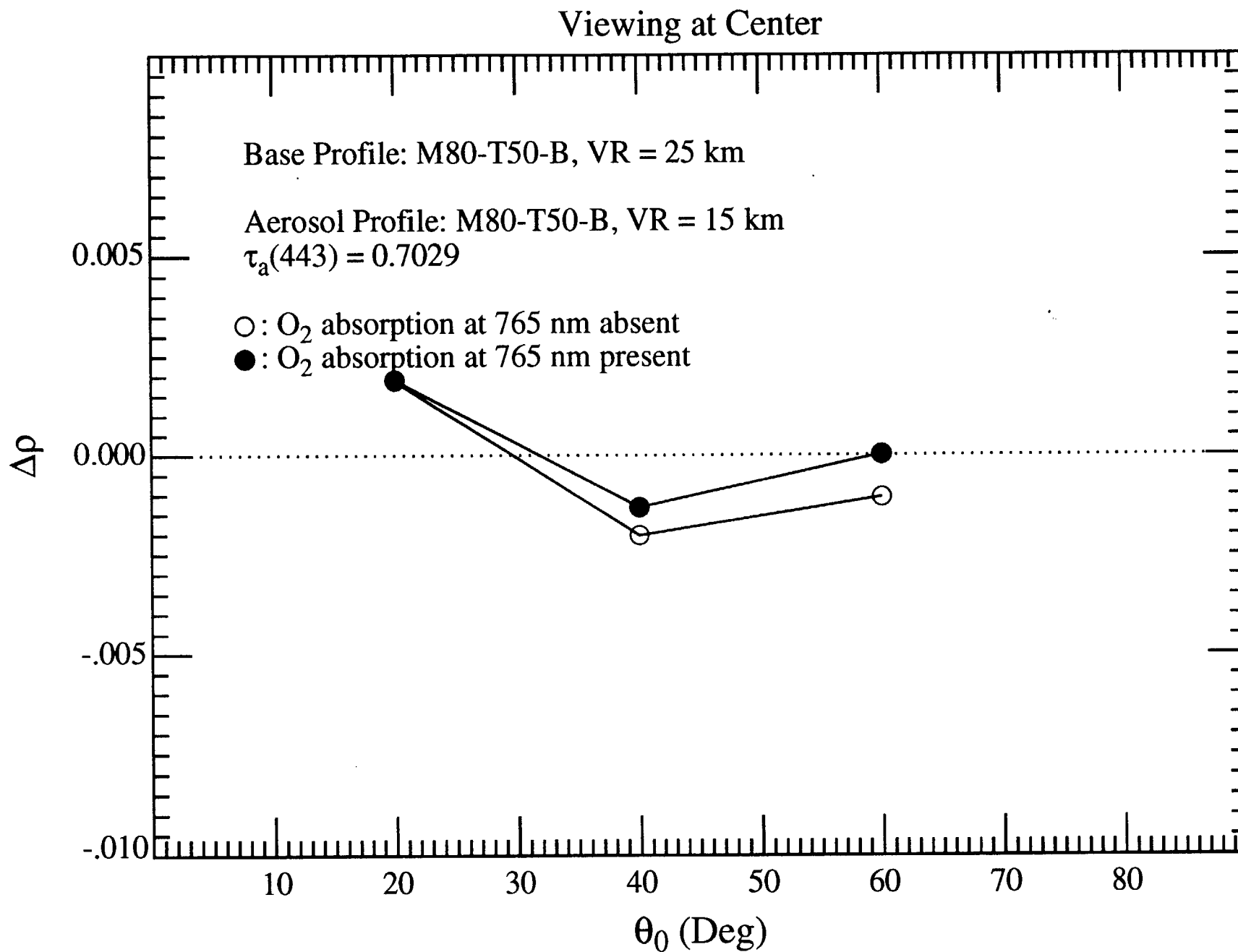


Fig. 10a

Viewing at Center

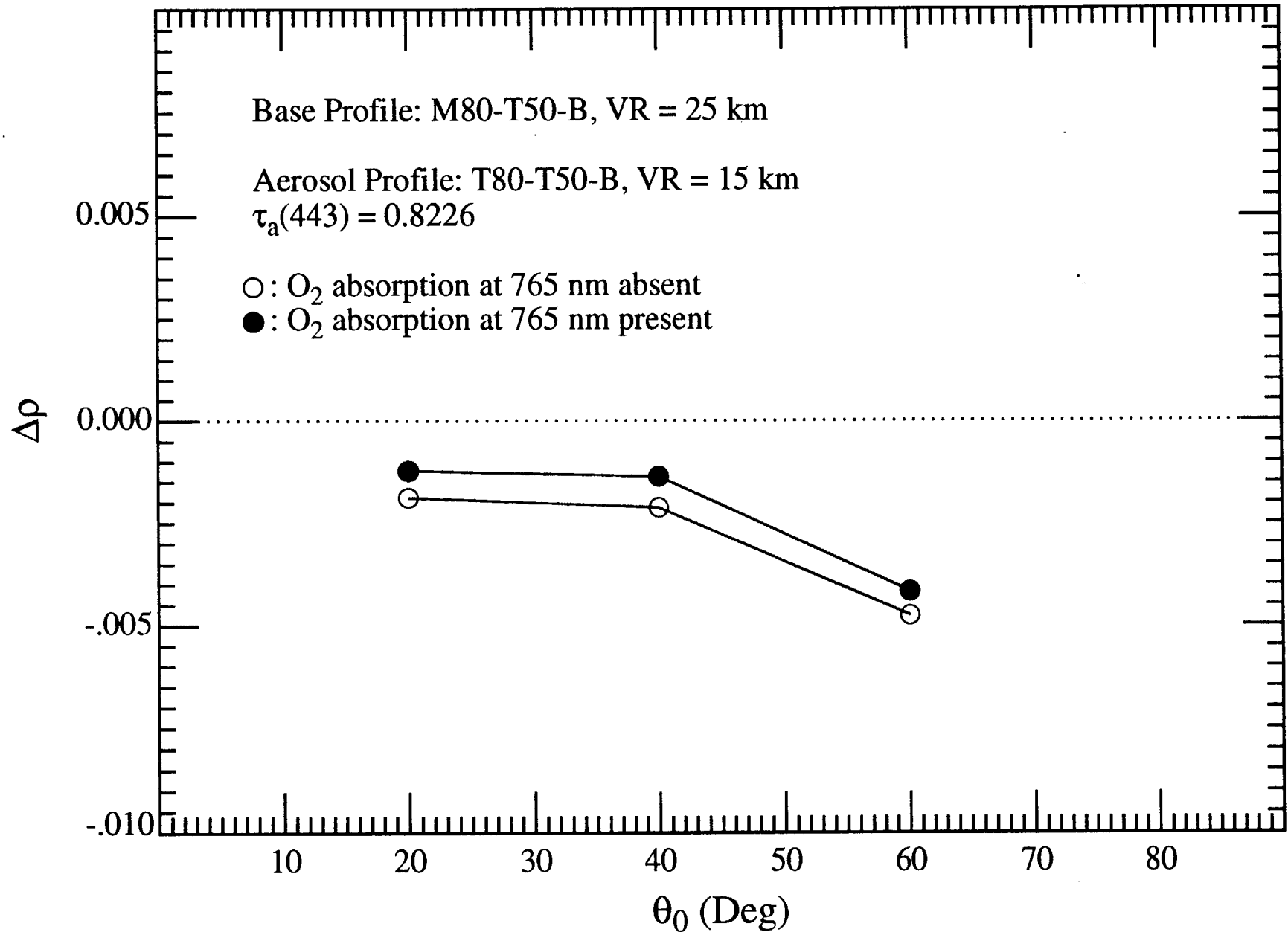


Fig 106

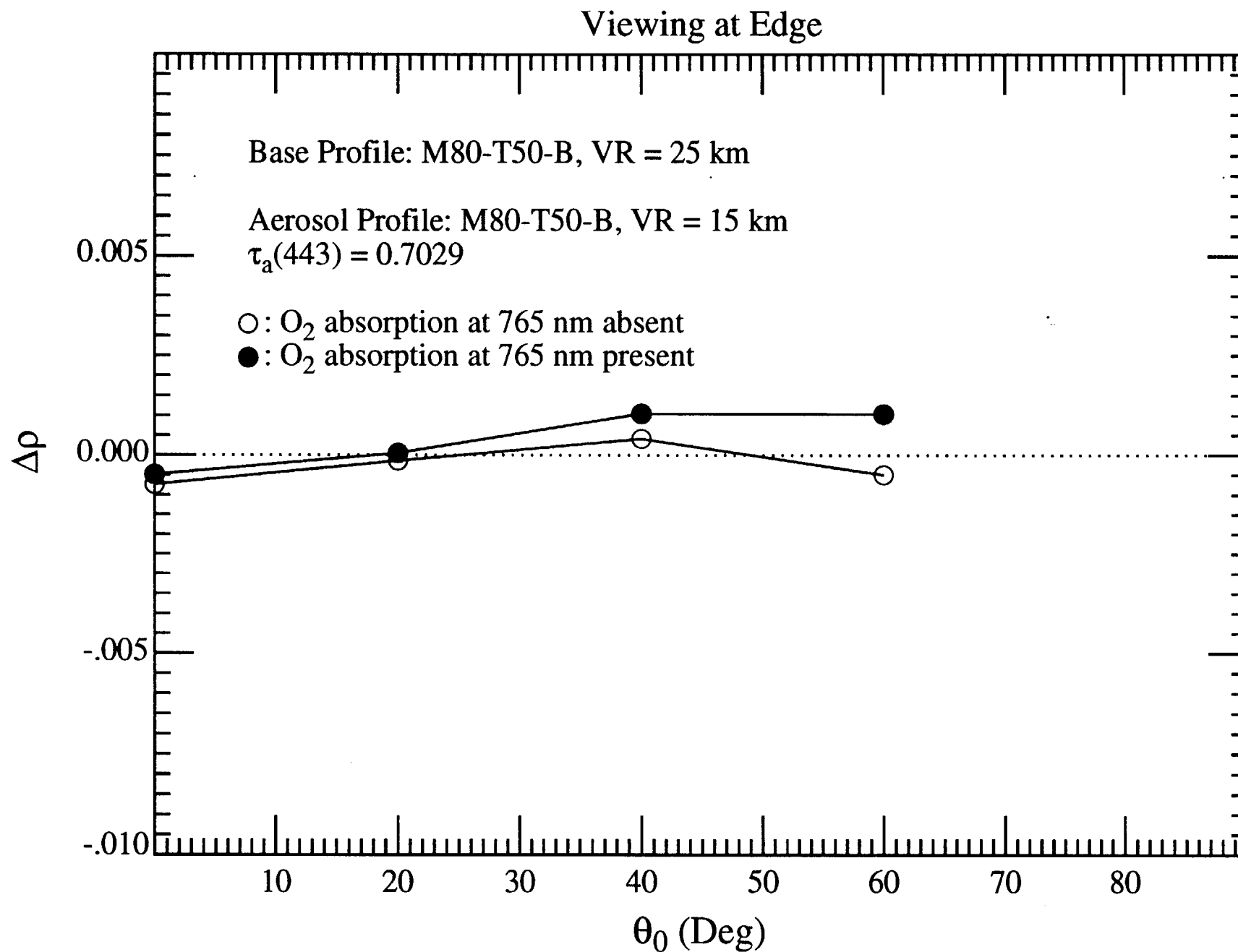


Fig 10c

Viewing at Edge

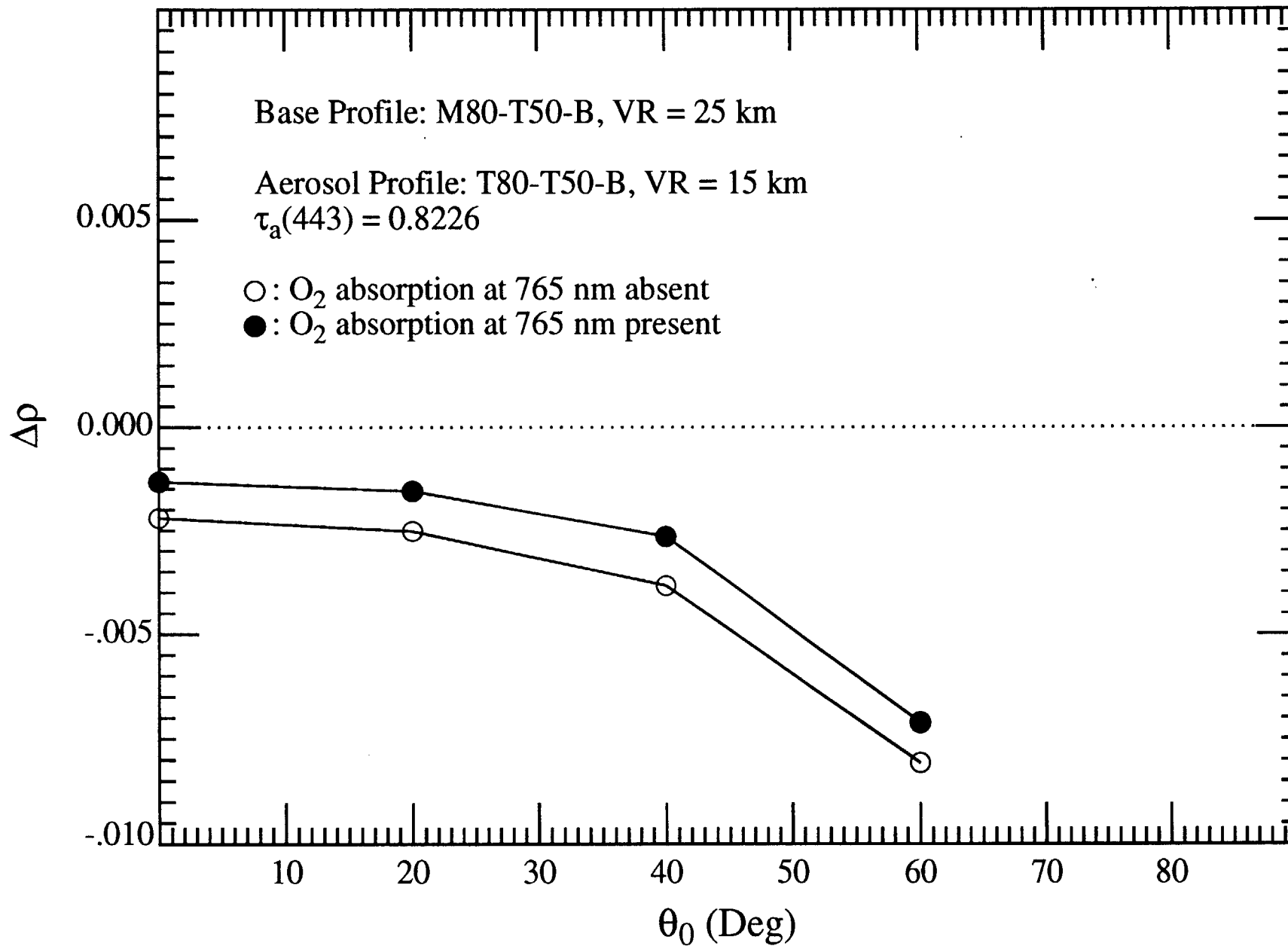


Fig 10d

Viewing at Center

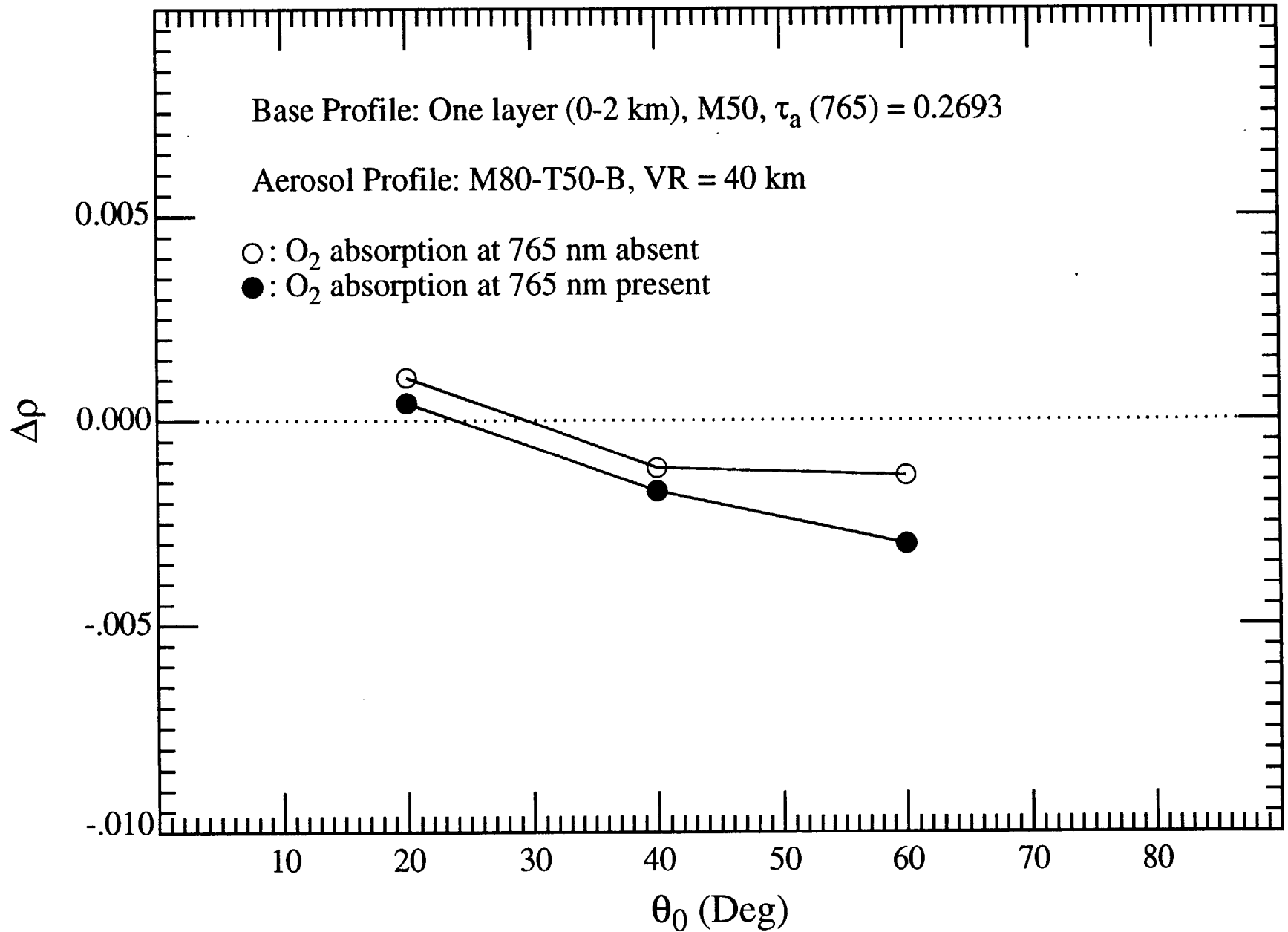


Fig. 11(a)

Viewing at Center

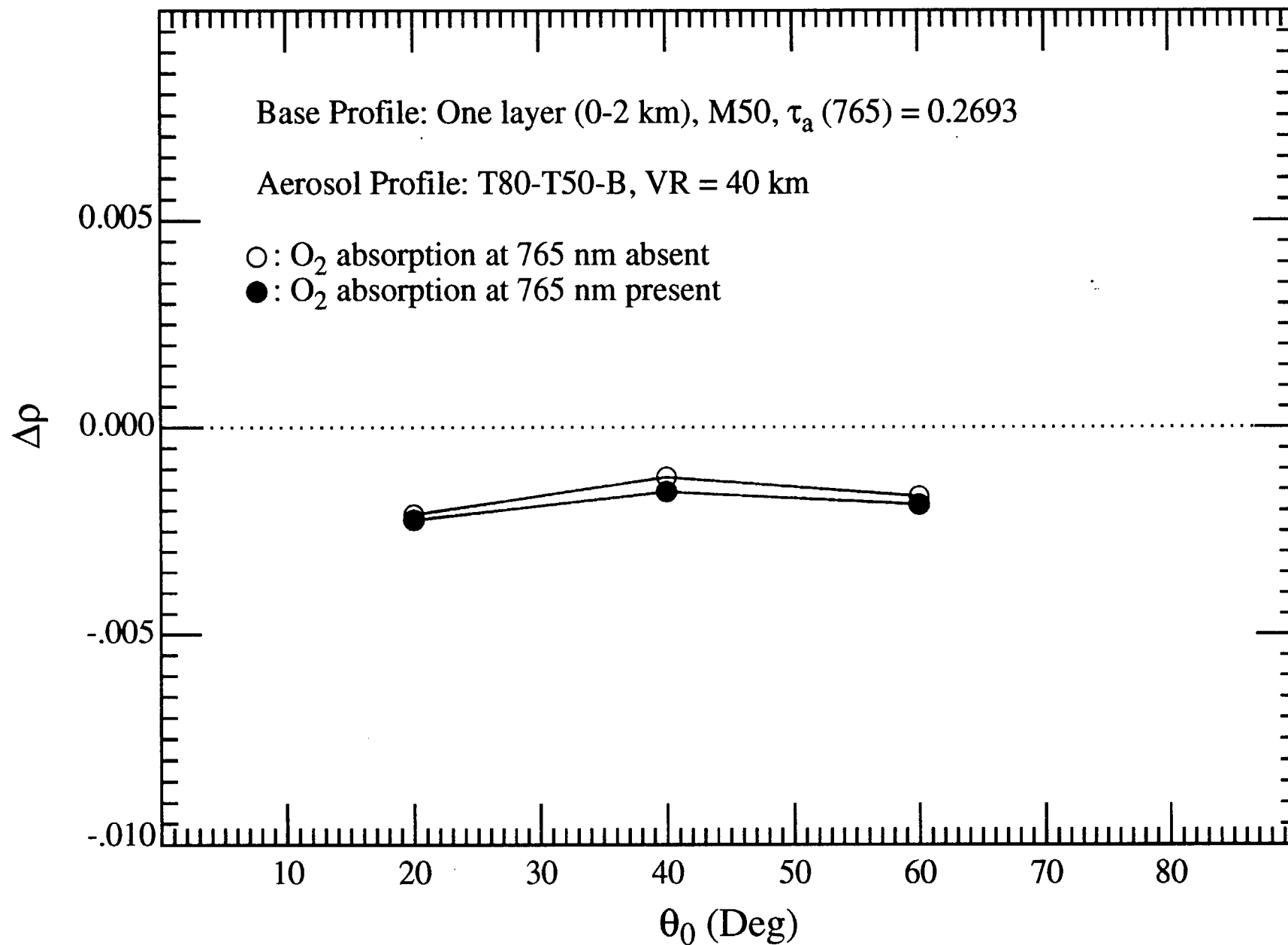


Fig. 11(b)

Viewing at Center

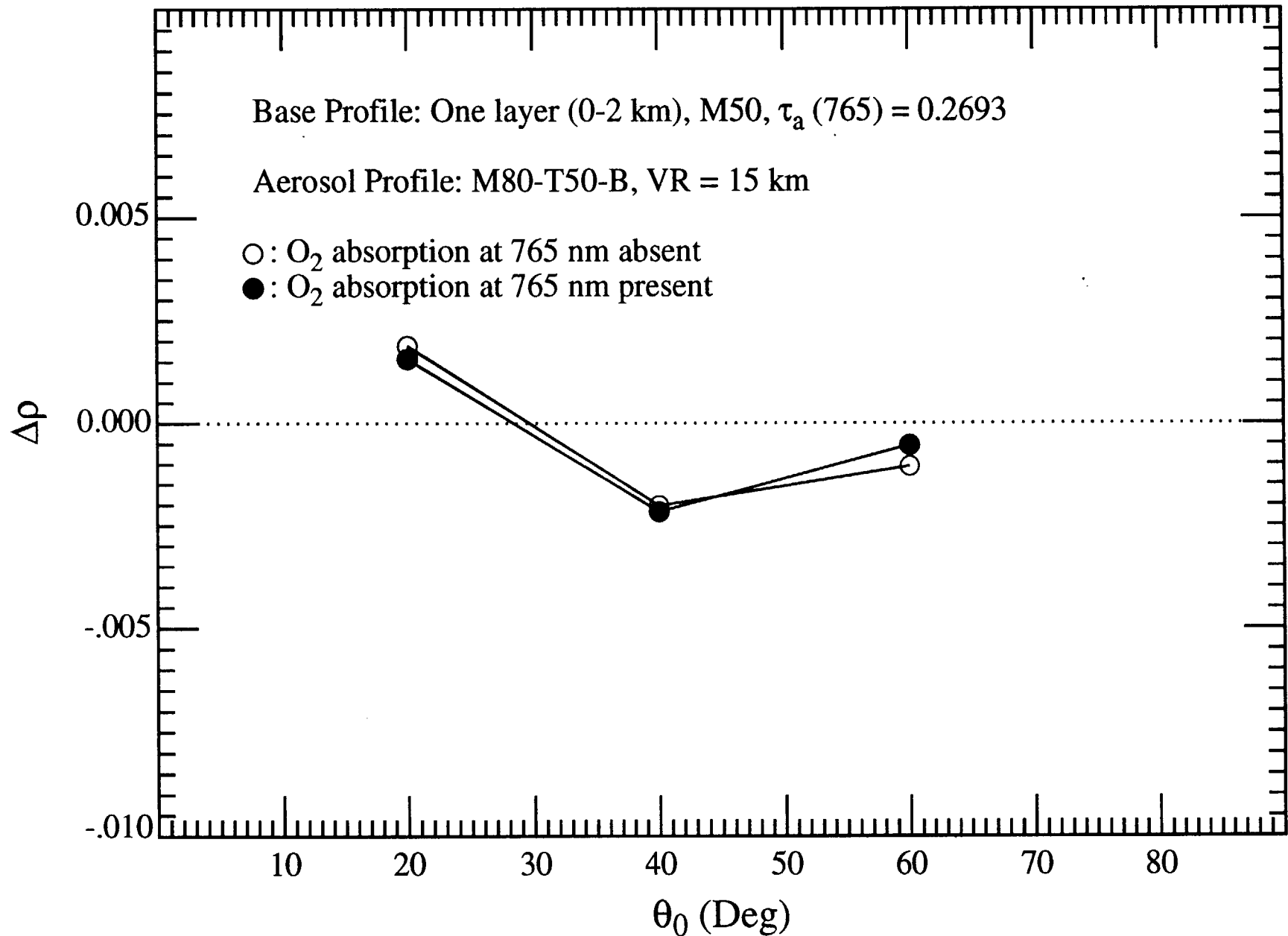


Fig. 11(c)

Viewing at Center

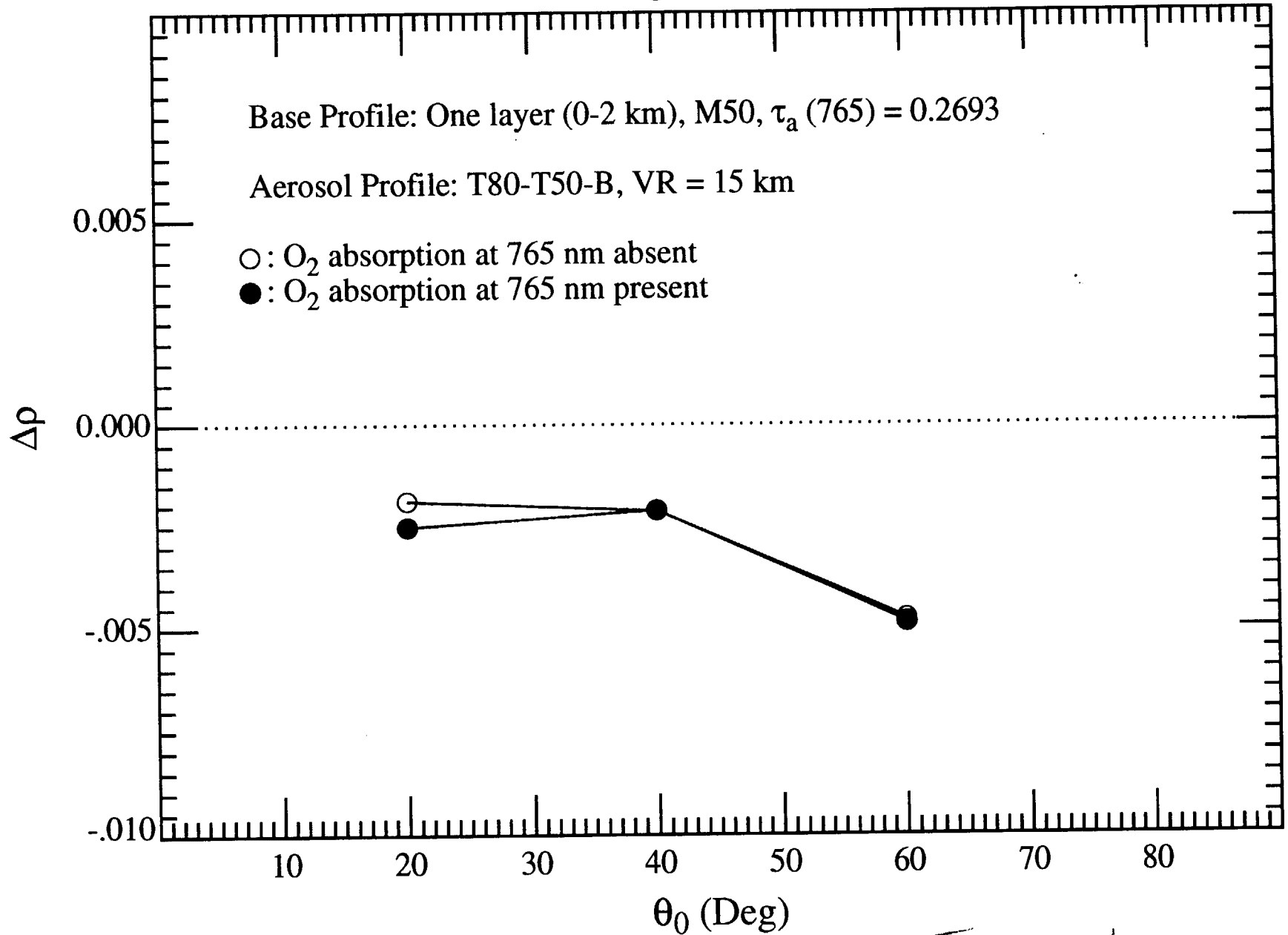


Fig. 11(d)

Viewing at Center

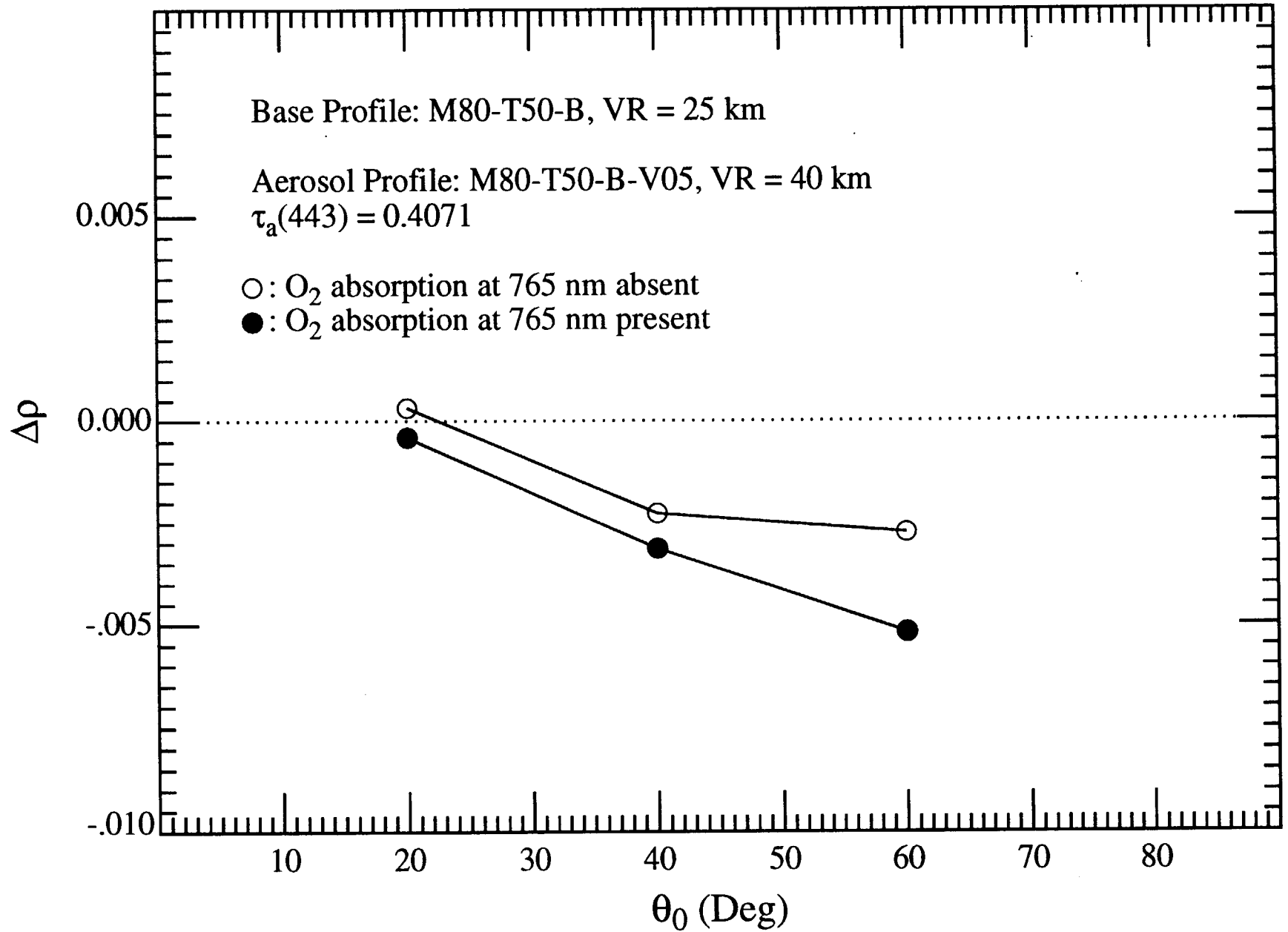


Fig. 12a

Viewing at Center

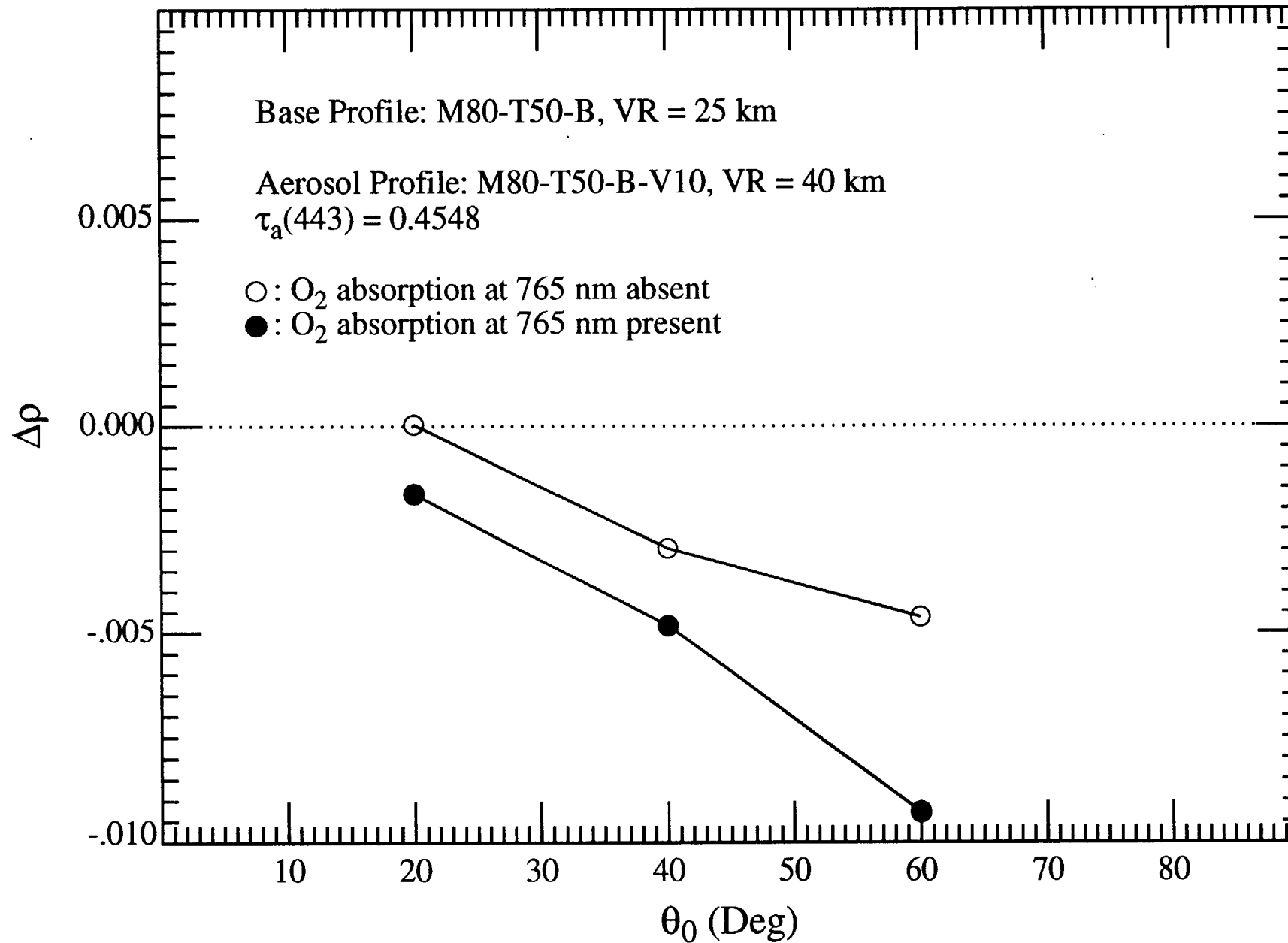


Fig 12b

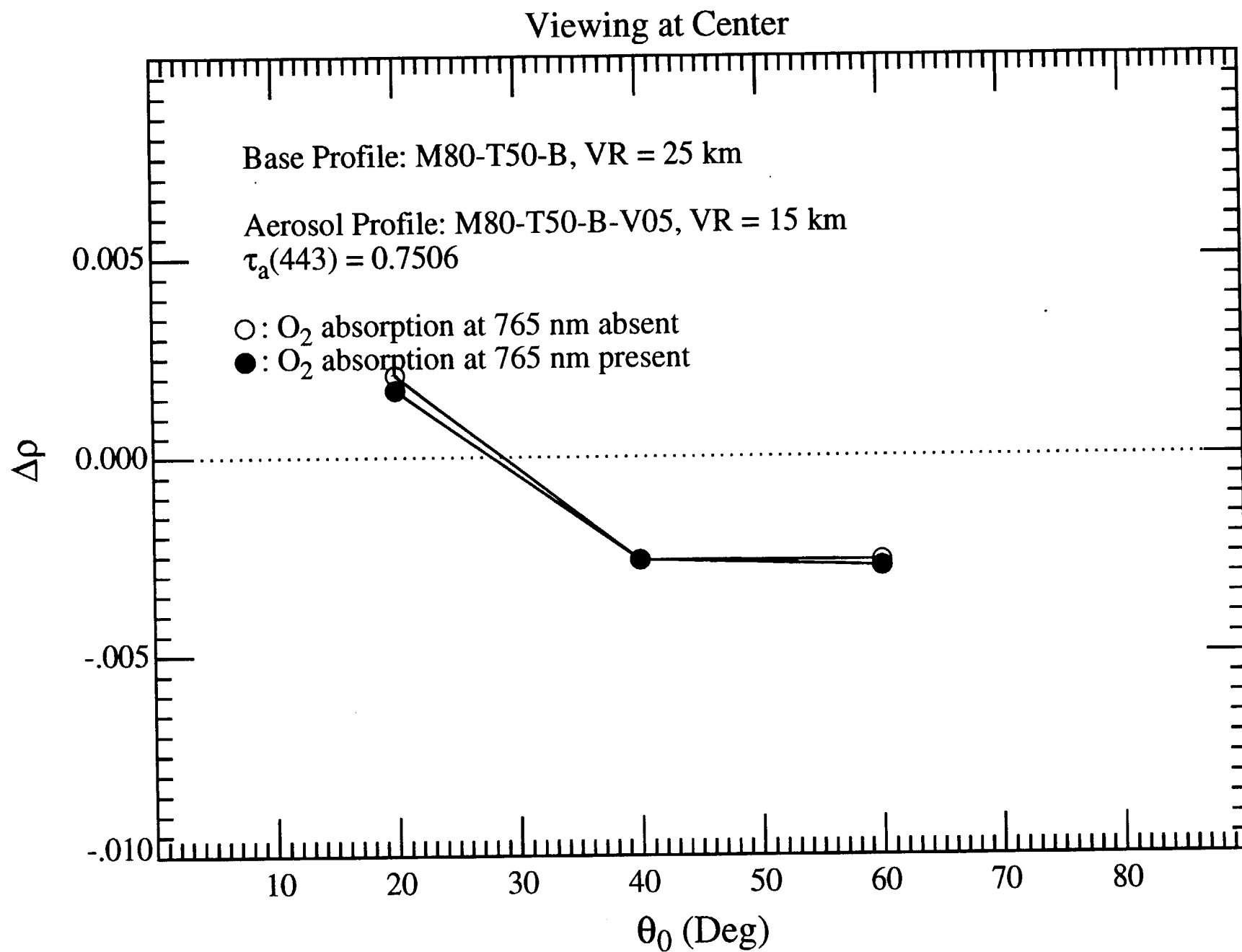


Fig. 12c

Viewing at Center

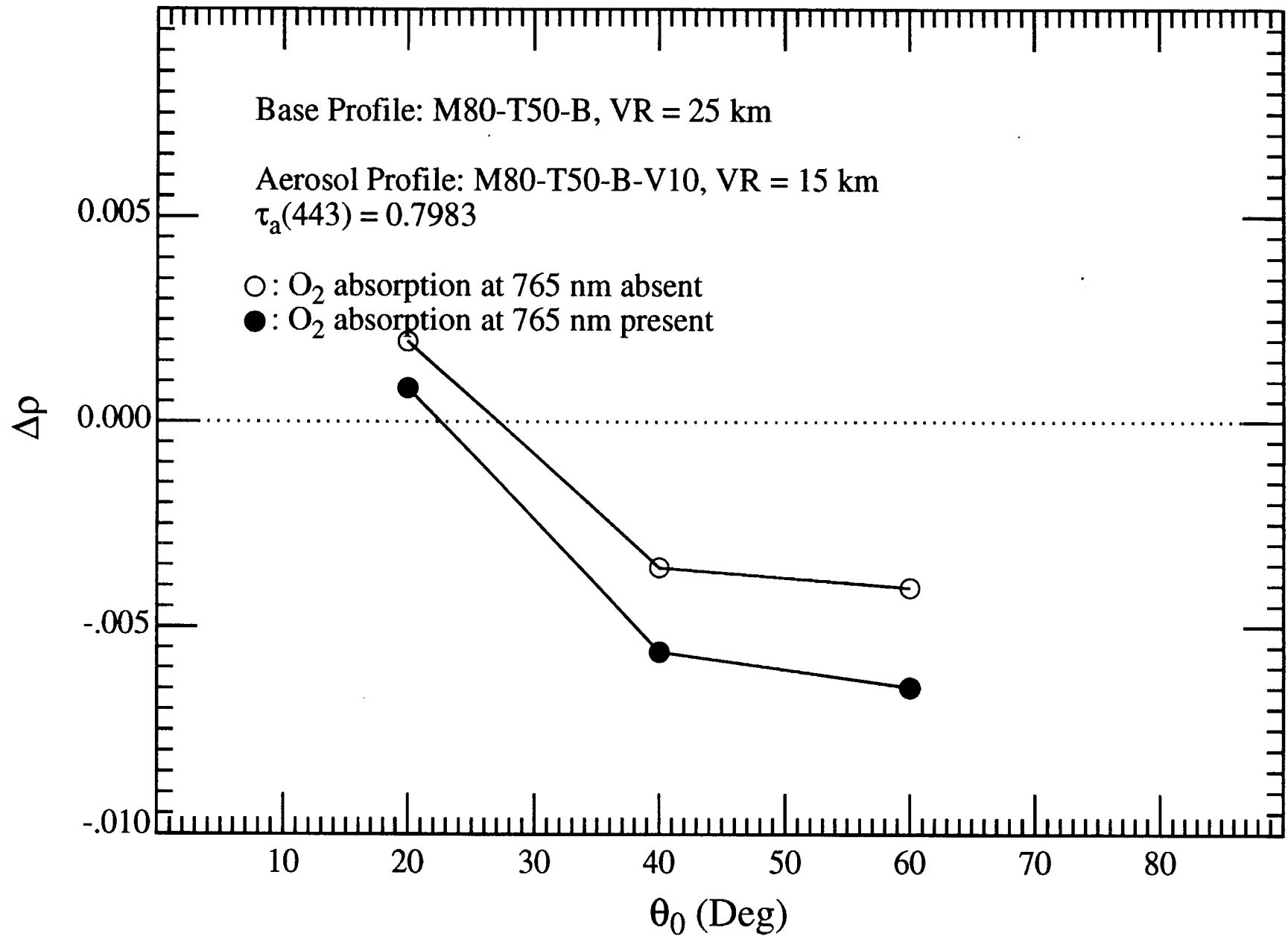


Fig. 12d